

Cite this: *J. Mater. Chem. A*, 2024, 12, 14334

Deciphering interfacial charge transfer mechanisms in electrochemical energy systems through impedance spectroscopy

Karamjyoti Panigrahi, Santanu Mal and Sayan Bhattacharyya *

Electrochemical energy conversion and storage systems have become an integral part towards a sustainable future, where the goal is to achieve high energy efficiency for each targeted application. The output of these devices is governed by the material design and the underlying interfacial chemistry at the junction of the electrode and the electrolyte. Electrochemical impedance spectroscopy (EIS) is based on the response of applied frequency to the modulated potential and the decoupled capacitive and resistive components. It has emerged as a versatile non-destructive analytical tool endowed with the benefits of differentiating between multiple solid/electrolyte and solid/solid interfaces. In this perspective, the model-based and model-free approaches are elaborated along with relevant case studies for elucidating the charge transfer at multiple interfaces for water electrolysis, CO₂ and N₂ reduction to value-added fuels, and ammonia, respectively, in addition to the metal-ion, metal-air and photo-rechargeable batteries. The avenues to minimize the charge transfer resistance for boosting the overall device performance are also discussed.

Received 24th January 2024
Accepted 8th May 2024

DOI: 10.1039/d4ta00537f

rsc.li/materials-a

1. Introduction

The depletion of non-renewable resources and the adverse environmental impact of fossil fuels have catalysed the pursuit of eco-friendly renewable energy.¹ The global energy demand has catapulted the utilization of renewable resources, triggering the research on developing practical solutions in electrochemical energy conversion and storage.² Besides the

electrocatalytic production of green H₂ by water splitting,³ the continuous greenhouse gas emission have spurred our interests to the electrochemical reduction of CO₂ (CRR or CO₂RR) to a myriad of carbon-based products, spanning from CO to multiple carbonaceous and hydrogenated products.^{4,5} Electrochemical methods to generate NH₃ under milder conditions have also garnered interest in order to circumvent the excessive energy consumption in the Haber-Bosch process.^{6,7} All these different reactions and parameters are connected by one string, *i.e.*, the electrode/electrolyte interface. Understanding the interfacial chemistry is a prerequisite to design champion

Department of Chemical Sciences and Centre for Advanced Functional Materials, Indian Institute of Science Education and Research (IISER) Kolkata, Mohanpur, 741246, India. E-mail: sayanb@iiserkol.ac.in



Karamjyoti Panigrahi

Dr Karamjyoti Panigrahi was working as a postdoctoral fellow in the Department of Chemical Sciences, IISER Kolkata, before joining as Senior Process Engineer in Cell System division of OLA Battery Innovation Centre, Bengaluru, India in September 2023. Prior to that, he obtained his PhD degree from Jadavpur University, Kolkata, and was a postdoc at IISER Pune, India in 2023. His research interests are in energy storage/conversion and halide perovskites.



Santanu Mal

Mr Santanu Mal is pursuing his PhD at the Department of Chemical Sciences, IISER Kolkata, India after completing his MSc degree in chemistry from IIT, Kharagpur, India, in 2019. Before that, he received his BSc in chemistry from Ramakrishna Mission Residential College, Narendrapur (Autonomous), University of Calcutta, India in 2017. His current research focuses on the development of metal halide perovskites in the field of optoelectronics and energy storage devices.

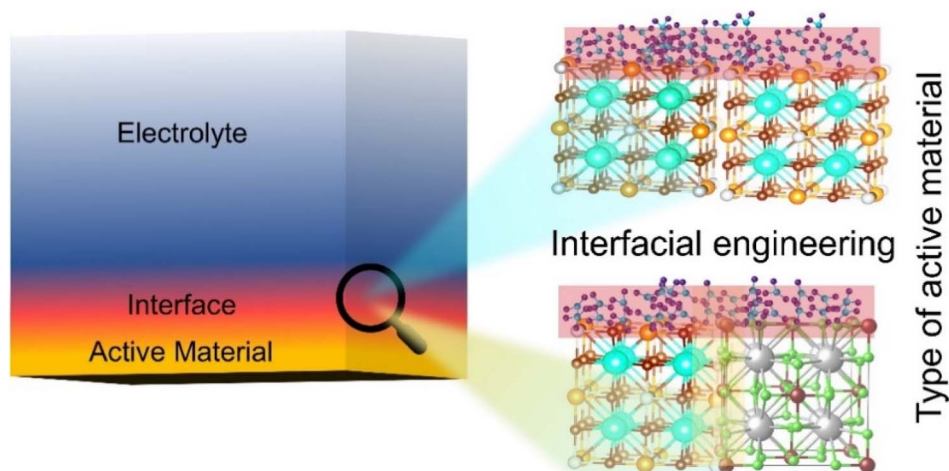


Fig. 1 Schematic representation of the electrode (active material)/electrolyte interface. When the active material consists of a single component, a single electrode/electrolyte interface is obtained (right, top). The presence of two active components in the electrode results in an additional interface between the two active materials (yellow shaded region, right, bottom).

catalysts in the respective fields. Heterointerfaces are equally indispensable for developing competent electrochemical energy storage devices, namely, the metal-ion, metal-air, and metal-oxygen/sulphur batteries.^{8,9}

The reaction kinetics at the electrode/electrolyte interfaces is not fully comprehended by traditional transient electrochemical measurements since it is unable to distinguish between the faradaic (where redox reaction occurs) and non-faradaic signals.^{10,11} This gap area is resolved by EIS because of its ability to distinguish between these two submerged components. In EIS, *electrochemical impedance* refers to the resistance of the AC/DC flow through an electrochemical system, and *spectroscopy* suggests an interaction between the matter and an excitation that results in a spectrum with frequency or wavelength as the measured parameters. Overall, EIS refers to the variation of resistance/impedance with respect

to the frequency of an electrochemical system under an applied AC potential. This AC perturbation helps to distinguish between the capacitive and resistive responses of electrode interfaces depending on the frequency-dependent current, which is otherwise difficult to manifest *via* the conventional electrochemical tests.

The review article on EIS revolves around the physical interpretation of impedance measurements in water splitting,¹² electrical double layer capacitor (EDLC)-based electrodes,¹³ in monitoring the quality of the proton exchange membrane of fuel cells,¹⁴ and for understanding the electronic properties of metal oxide electrodes in electro/photocatalysis, ion batteries and heterojunction solar cells.¹⁵ In photo-assisted electrochemical reactions, EIS analysis helps in unravelling the role of electron-hole diffusion, carrier recombination, surface defects, and trap states in solar cells, along with the passivator at the solid-electrolyte interface. By coupling the physics and chemistry aspects, graphical methods have been used to develop and analyse the models with error (stochastic and bias) analysis, specifically in the corrosion, battery and biological fields.¹⁶ In addition to the elucidation of the distribution of relaxation times,¹⁷ a better understanding of the impedance spectra can be obtained by unravelling the charge transfer at multiple junctions of the electrochemical device (Fig. 1). When multiple active materials are present on the electrode surface, additional interfaces are created, and the charge transfer resistance (R_{ct}) at each of these interfaces has a profound impact on the overall electrochemical performance. In the following sections, we start by providing a background on EIS analysis, the nature of impedance of each electrical component, and the basic circuits (Table 1). The significance of the equivalent circuit model (ECM), transmission line model (TLM), and model-free approach has been elucidated. Specific case studies are covered in the context of water electrolysis, CO₂ and NH₃ reduction, and electrochemical storage systems, namely,

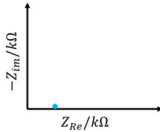
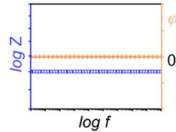
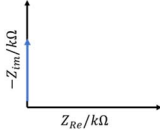
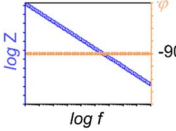
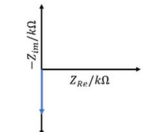
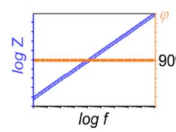
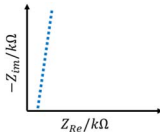
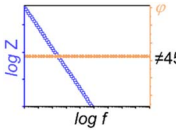
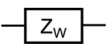
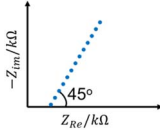
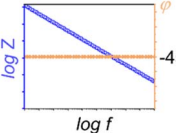
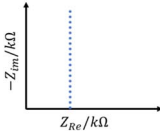
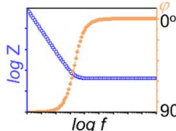
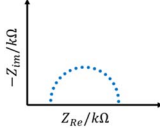
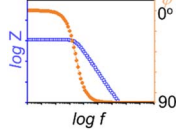


Sayan Bhattacharyya

Prof. Dr. Sayan Bhattacharyya is working at the Department of Chemical Sciences, IISER Kolkata, India. He received his PhD degree from Indian Institute of Technology (IIT) Kanpur, India, in 2006. After two postdoctoral stints at Bar-Ilan University, Israel (2006–2008) and Drexel University, USA (2008–2010), he joined IISER Kolkata as Assistant Professor in April, 2010. He is currently a full Professor and was also the founder Chair of the

Centre for Advanced Functional Materials at IISER Kolkata. He is a solid-state chemist interested in nanoscience, catalysis for energy conversion and storage, and hybrid perovskite photovoltaics and optoelectronics.

Table 1 Different components and circuits along with the representative standard Nyquist and Bode plots

Electrical components	Symbol/circuits	Nyquist plot	Bode plot
Resistance $Z_R = R$			
Capacitance $Z_C = \frac{1}{j\omega C}$			
Inductance $Z_L = j\omega L$			
CPE $Z_{CPE} = 1/(j\omega)^{\beta} Q$			
Warburg impedance $Z_W = \frac{\sigma\sqrt{2}}{(j\omega)^{1/2}}$			
Series connection $Z_t = R + 1/j\omega C$			
Parallel connection $Z_t = \frac{R \times \left(\frac{1}{j\omega C}\right)}{R + (1/j\omega C)}$			

metal-ion, metal-air/O₂, and the photo-rechargeable batteries. We portray the importance of materials design as a key factor in minimizing the R_{ct} for better electrochemical performance.

2. Basics of EIS

EIS is an integrated technique where an AC perturbation with small amplitude, $|E_0| \sim 5\text{--}10$ mV, is coupled with the applied potential $E(t)$. The overall modulation is subsequently investigated at a controlled angular frequency (ω), following eqn (1). The EIS plot is obtained by converting ω into the linear mode, *i.e.*, $\omega = 2\pi f$, where f is the frequency in Hz. A small potential E_0 is a prerequisite for maintaining the linear current behaviour, according to the Butler-Volmer model (eqn (2)).¹⁸ Both $E(t)$ and $I(t)$ are in the same frequency but $I(t)$ has an additional offset, the phase angle (φ). In an AC circuit, the impedance $Z(\omega)$ is the ratio of the alternating potential and current (eqn (3)), which is equivalent to the DC resistance in ohm (Ω).

$$E(t) = |E_0|e^{j\omega t} \quad (1)$$

$$I(t) = |I_0|e^{j(\omega t + \varphi)} \quad (2)$$

$$Z(\omega) = E(t)/I(t) = \frac{E_0}{I_0}(\cos \varphi - j \sin \varphi) \quad (3)$$

The modulated frequency is typically sampled over 1 mHz (or 0.5 mHz) to 1 MHz under a constant applied potential (E_{app}), along with a small modulation/perturbation (E_0). Therefore, the total applied potential (E_t) becomes $E_{app} + |E_0| \sin(\omega t)$. After the completion of measurement, the magnitude of E_{app} changes, and thereafter the process is repeated.

The data is interpreted by the Nyquist and Bode plots. In the Nyquist plot, the impedance is plotted considering $j = \sqrt{-1}$ according to eqn (4). $Z_{Re}(Z')$ and $Z_{im}(Z')$ are taken in the x - and y -axes, respectively. Conventionally, each data point denotes a separate frequency, where ω decreases from left to right. The

applied potential remains constant at low frequencies, and this potential is considered the DC limit of the system where the real part of the impedance Z' is the summation of two resistances, solution resistance (R_s) and R_{ct} ; $Z' = R_s + R_{ct}$. The impedance at a specific frequency can be calculated individually by considering a vector from the origin, having magnitude $|Z| = \sqrt{Z'^2 + Z''^2}$ and phase angle $\tan \varphi = Z''/Z'$.

$$Z(\omega) = |Z|(\cos(\varphi) - j \sin(\varphi)) = Z' - jZ'' \quad (4)$$

The maximum point in the Nyquist plot is related to the interfacial capacitance (C_{int}) and R_{ct} . Maintaining the phase angle φ , if a slope is drawn from the origin of the Nyquist plot, then the point touching the semicircle provides the frequency (f_p), which is equivalent to $1/R_{ct}C_{int}$. $R_{ct}C_{int}$ depicts the time constant of a circuit where the electrical components are connected in parallel. The current passing through the electrode/electrolyte interface can be divided into faradaic and non-faradaic components, quantified by R_{ct} and C_{int} , respectively. In the Bode plot, a double y-axis contains $|Z|$ (first y-axis) and φ (second y-axis), plotted against the modulation f in the x-axis. It provides information at a unique frequency in each data point. The Bode plot can also be plotted separately as Bode- Z ($|Z|$ versus f) and Bode-phase plots (φ versus f) containing the same information as the single Bode plot. Similar analysis can be carried out using $\log|Z_{Re}|$ and $\log|Z_{Im}|$ vs. $\log(f)$. Understanding R_{ct} is vital for comprehending the charge transfer across hetero-interfaces, yet the roles of other circuit components such as the series resistance, representing the overall resistance, and the Warburg impedance (Z_W), indicating the diffusion resistance, are equally pivotal.

3. EIS modelling components

3.1 Resistor

The faradaic charge transfer across the interfaces is described by the resistors, where the impedance of a resistor (Z_R) is the resistance (R in Ω , Table 1). Although the mobile charges across the solid and liquid phases generate the resistance, the diffusive elements allow the better modelling of these characteristics. It is a real and frequency-independent term and will always be on the real axis (Z'), irrespective of the electrochemical reaction. In case of the Bode plot, as there is no phase shift between the current and applied voltage, the value is frequency-independent, parallel to $\log f$.

3.2 Capacitor and constant phase element (CPE)

The non-faradaic charge accumulation at the solid/solid and solid/liquid interfacial layers is modelled as capacitance considering the variation of the dielectric medium in the parallel plate configuration. The interfaces within the heterostructured electrocatalysts and between the catalyst and the underlying substrate behave like capacitors. To explain the solid/solution interface, the capacitance is frequently correlated with the density of electronic states at the catalyst surface. The impedance of a capacitor (Z_C) maintains a relationship with ω by the relation

$Z_C = 1/j\omega C$; therefore, Z_C is most significant at lower frequencies and small at higher frequencies. In the Bode plots, the capacitive current lags 90° behind the applied potential. The capacitance often shows a nonideal behaviour at the double-layer of the solid/electrolyte interface because of the complexity in the double-layer, surface imperfections, and porosity of the electrodes. As a result, CPEs are frequently used for modelling such interfacial layers. The impedance of a CPE is expressed by $Z_{CPE} = 1/(j\omega)^\beta Q$, where Q denotes the nonideal capacitance ($Fs^{\beta-1}$), and the ideality factor (β) is between 0.8 and 1.

3.3 Inductor

The inductor is generated by the proximal metallic contacts, and the close vicinity of cathodes and anodes in a trim device configuration, for example, between the sandwiched electrodes in the heterojunction solar cells. Unlike the capacitance, the impedance of an inductor (Z_L) is directly proportional to ω ($Z_L = j\omega L$). The presence of an inductive circuit element is confirmed by observing the real part cross-over in the Nyquist semicircle at low f (Z_{Im}).

3.4 Warburg impedance

Z_W results from the resistance to the diffusion of mobile charges. In a finite thickness layer, Z_W can be categorized in two parts, finite length Warburg or open contacts (Z_{W0}) for corrosion processes and finite space Warburg or shorted contacts (Z_{WS}) for metal-ion batteries. For Z_{W0} , one boundary imposes a fixed concentration of species, making it permeable for diffusion, whereas in the case of Z_{WS} , one boundary blocks the diffusion species. The relation between Z_W and ω can be expressed as $Z_W = \sigma(\omega)^{-\frac{1}{2}}(1-j)$, where σ is the diffusion resistance. At high frequencies, Z_W is small as diffusive reactants do not move far away from the electrode. A characteristic linear relationship exists between Z' and Z'' , and for the Nyquist plot, $\varphi = -45^\circ$ and slope = 1. The slope -45° is due to the equal real and imaginary parts [$Z'_W = Z''_W$]. When the diffusion coefficient (D) decreases, the supply of active species to the electrode surface area is reduced, increasing Z_W , and thereby shifting the straight line to the low frequency region in the Bode plot (Table 1). The lifetime of diffusion is denoted by $\tau_d^{1/2} = L/D^{1/2}$, where L is the finite thickness of the diffusion layer.

3.5 Randles circuit

The Randles circuit helps to model the flow of current through an electrode interface (Fig. 2a). The flow of current, faradaic or non-faradaic, through the interface is described by R_{ct} and interfacial (or double layer) capacitance (C_{int}/C_{dl}), respectively. The electrode may consist of a solid/solid or solid/liquid interface, depending on the electrochemical system. R_{ct} is associated with the faradaic processes, involving electron transfer reactions. The electrode behaves like a resistor in the low overpotential range <10 mV. The formation of a capacitive layer on the electrode surface *via* the solvated ion interaction introduces C_{dl} as a parallel component, which involves the non-faradic current flow. The first resistor connected in series (R_{series}) is

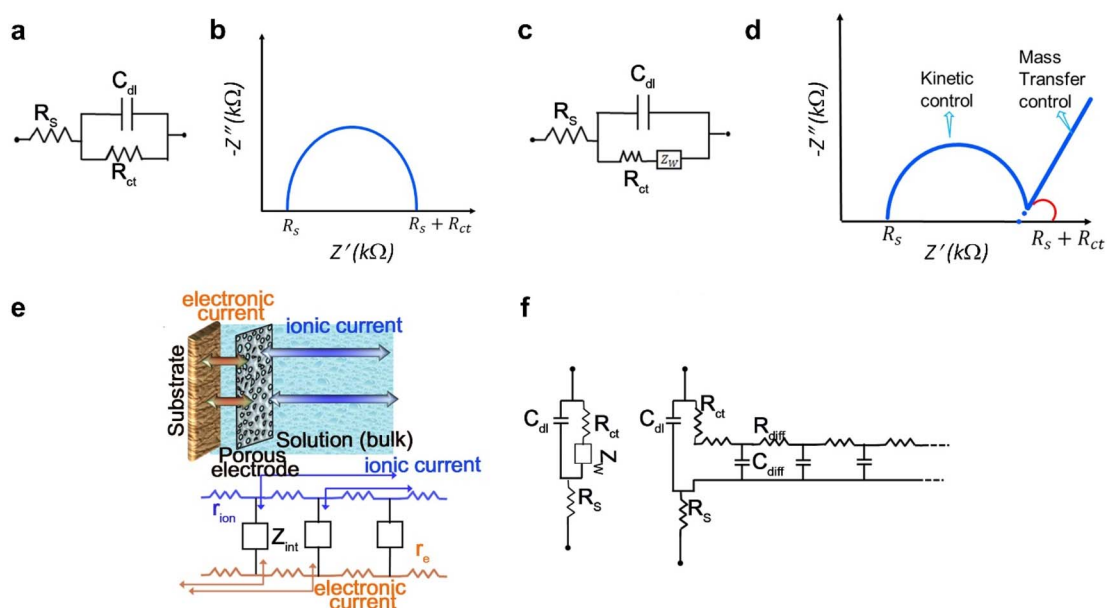


Fig. 2 (a) The simplified Randles circuit and (b) the typical Nyquist plot. (c) Randles circuit with the Warburg diffusion element and (d) the corresponding Nyquist plot. (e) Electronic and ionic currents in the case of porous electrodes (top) and the generated resistance due to these two components (below). (f) The conversion of conventional Randles circuit to equivalent TLM, where the Warburg diffusion element (Z_w) is replaced by two parallel components, R_{diff} and C_{diff} .

the resistance associated with the electrolyte, wires, and contacts. At high frequencies, the C_{dl} will be minimum, and the current will pass through the capacitor and not the resistor R_{ct} . The total impedance will be a summation of R_s and other factors due to C_{dl} . As C_{dl} becomes maximum at low frequencies, the current will pass through R_{ct} . In that case, the total impedance will be $R_{series} + R_{int}$. A semicircle with diameter equal to R_{ct} is thus observed in the Nyquist plot (Fig. 2b). In reality, the scenario is different since the faradaic reaction is tailored by the diffusion of the electrolyte ions to the electrode surface. This phenomenon is more prominent, particularly in the low frequency region, where the electrolyte ions get enough time to diffuse within the electrode surface, giving rise to a slope along 45° with the semicircle (Fig. 2c and d). Accordingly, the circuit is modified by connecting a diffuse resistance element, *i.e.*, Z_w , in series with R_{ct} since it affects the overall charge transfer (Fig. 2c). To select an appropriate EIS model, interpretation hinges on discerning individual electrical components within the Nyquist plot. Each interface and its associated electrochemical reaction must be considered to construct an equivalent circuit model. The optimal approach to model interfacial charge transfer involves coupling the logically chosen equivalent circuit with the specific electrochemical reaction of interest.

4. EIS models and data analysis

4.1 Transmission line model (TLM)

The model-based approach, namely, the ladder-like circuit or TLM, is utilized to describe the interaction between electrolyte ions and the porous electrode.^{19,20} Porous electrodes consist of

an electroactive material and the impregnated electrolyte ions, governed by the electronic and ionic conduction, respectively, which gives rise to two opposite flowing currents. The impedance at the porous electrode/electrolyte interface can be represented by the interfacial impedance (Z_{int}) (Fig. 2e). Since Z_w is related to the ion diffusion gradient, it can be modelled as a linear model of R and C components (Fig. 2f).¹⁹ The TLM model is useful in deriving the transport and reaction parameters, namely, the concentration of mobile carriers, chemical diffusion coefficient, exchange current density, and the capacity of solid electrolyte interphase layer, from a knowledge of the geometry of different surface layers, their thickness and surface area. The only limitation of the TLM model is the requirement of a porous electrode.

4.2 Model-free approach

The model-based ECM and TLM approaches depend on a prior knowledge regarding the impedance of the investigated system, and this gridlock may lead to multiple circuits for the same impedance data.²¹ In the model-free distribution function of relaxation time (DFRT) or distribution of relaxation time (DRT) method, the relaxation time is associated with the time constant, *i.e.*, the RC component of the circuit. It displays the amount of time needed for the electrochemical systems to change from one equilibrium state to another under external perturbation. It describes the distribution of relaxation times and precludes the requirement of any prior knowledge of the investigated system. The obtained EIS data is at first processed *via* impedance spectroscopy genetic programming (ISGP) in order to acquire the functional form of the distribution of relaxation time.²¹ The model consists of time-domain peaks

that can be linked to various polarization resistance-related phenomena. ISGP enables graphical monitoring to find the independent parameters, circumventing the use of any filter or Lagrange coefficients and the tracking of each separated convoluted peak.^{22,23} The relation between the distribution function of relaxation times $\gamma(\tau)$ and the complex impedance $Z(\omega)$ with relaxing time constant is:

$$Z(\omega) = R_{\infty} + R_p \int_{-\infty}^{\infty} \frac{\log(\tau)}{1 + j\omega\tau} d(\log(\tau)) \quad (5)$$

where R_{∞} and R_p denotes the ohmic resistance (or series resistance) and total polarization resistance, respectively. τ signifies the relaxation time, and ω is the angular frequency. Eqn (5) is an ill-posed inverse problem, which requires advanced numeric programming to extract the information.²⁴ A developed MATLAB program, *i.e.*, ISGP, has been explored using an evolutionary algorithm, whose function is divided into checking and confirming the parts (Fig. 3).

The DFRT models comprise the linear combination of mathematical functions, which are scrutinized based on the “fitness function” and works based on its compatibility with the measured data.²⁵ A DFRT model, including Gaussian, Lorentzian, and other mathematical peaks, is the final product of the analysis. With each relaxation time, height, and width of the peaks for any polarization process, a typical DFRT model is plotted as a function of $\log(\tau)$. The larger the polarization, *i.e.*, the larger the semicircle in the Nyquist plot, the higher the peak area. The peak area is then multiplied by the total polarization resistance (R_{pol}) providing the polarization resistance of the specific electrochemical process. The total of all the peak regions in the DFRT model equals R_{pol} for a sufficiently wide bandwidth. Finite element modelling is another useful approach, in which the electrochemical processes are first

calculated on the local scale base and then mathematically summed upon for the entire electrode.²⁶

4.3 Data quality and reliability assessment

The extent of reliability of the impedance measurement is guided by the potentiostatic or galvanostatic modulation, frequency range, amplitude perturbation, and cycles per measured frequency. While the galvanostatic mode involves applying a current perturbation and measuring the potential response, it is just the opposite of the potentiostatic mode. The two modes can be identified from the steady-state current *versus* potential curves, prior to the EIS measurement. In case of a current–potential curve with a very sharp slope, the galvanostatic mode is more accurate and is beneficial when the impedance is low at high current densities. An electrochemical system with a large impedance can be accurately evaluated by the potentiostatic mode, where the current or potential amplitude is small in order to maintain a linear response but large enough to obtain the best signal-to-noise ratio. The electrochemical processes consist of different reactions, and hence the perturbation amplitude may not be the same in the entire frequency range, which necessitates different amplitudes to be adapted at different frequencies to avoid artefacts in the EIS data. In a frequency range of 10 kHz to 10 mHz, equally spaced logarithmic points >5/decade need to be employed for measuring the impedance spectrum with sufficient accuracy, where the number of cycles per frequency is vital to avoid the inherent error, particularly in the high-frequency region. The impedance data consists of three errors, namely, fitting (ϵ_{fit}), stochastic (ϵ_{stoch}) and bias (ϵ_{bias}). ϵ_{fit} is the residual error and is primarily governed by the inadequate circuit model selection, whereas ϵ_{stoch} has zero mean value and can be attuned by the

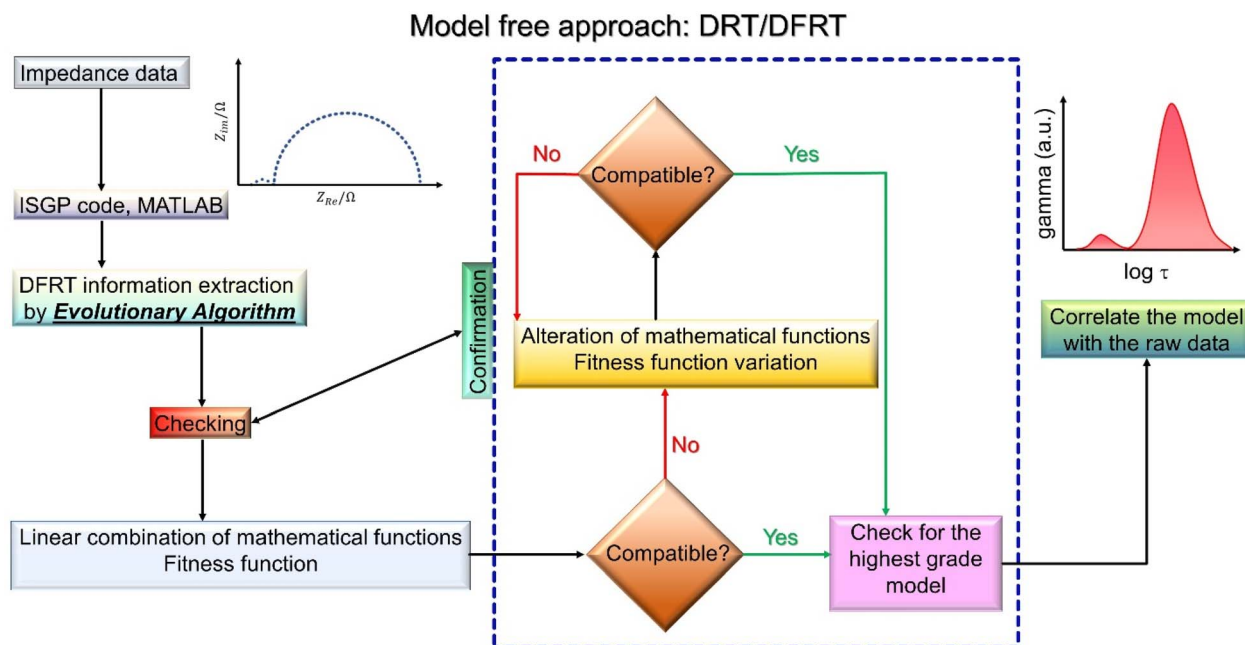


Fig. 3 Flowchart of the model-free approach for the estimation of impedance, DFRT or DRT.

standard deviation process, and $\varepsilon_{\text{bias}}$ occurs due to the inconsistent impedance data according to the Kramers–Kronig relation.²⁷ Impedance is also sensitive to temperature and external electromagnetic field; hence, to ensure reliable and repeatable data, necessary precautions should be taken into account, such as tight temperature control and emf-shield protection. However, ensuring data reproducibility is a prerequisite before applying the model-based or model-free analyses.

5. Electrochemical energy conversion

5.1 Water electrolysis to green hydrogen

Water electrolysis needs a thermodynamic potential of 1.23 V corresponding to a high energy input of $\Delta G = 237.1 \text{ kJ mol}^{-1}$.²⁸ Due to the sluggish kinetics of hydrogen evolution reaction (HER) and oxygen evolution reaction (OER), the electrocatalysts typically need overpotentials more than 1.23 V to reach the desired current density. In acidic medium, noble metal-based catalysts, for example, IrO_2 or RuO_2 for OER and Pt for HER, are considered as the benchmark, whereas in alkaline medium, transition metals, *e.g.*, Ni-based catalysts, exhibit a reliable performance.^{29,30} Besides the pursuit of an outstanding catalytic activity, the minimization of R_{ct} at the electrode/electrolyte is equally pertinent.³¹ The schematic in Fig. 4a represents the EIS investigation of the catalyst, where R_s , R_{ct} and C_{dl} are elucidated at the interfaces because of the transfer of electrons from the electrolyte to the electrode as well as ion diffusion within the pores of the electrode. Apart from solid–liquid (or solid–solid) interfacial interaction, R_{ct} is directly correlated to the catalyst's morphology,³² electrochemical active surface area (ECSA),^{33,34} active facets,³⁵ defects,^{36,37} interfacial band structure in between the catalyst and the bottom electrode,³⁸ and electron transport resistance and charge accumulation (Fig. 4b). Also, in multi-component electrocatalysts, the Fermi energy levels of individual phases tend to align themselves by altering the electronic environment, which has an important role in modulating the electronic charge transfer³⁹ and elevating the carrier transport.⁴⁰ This charge transport can be facilitated by the direct growth of the catalyst on the electrode surface, generating self-supported electrodes, thereby avoiding polymer binders or conductive additives.⁴¹

A pH-universal HER-active heterostructured electrode was designed by wrapping NiV layered double hydroxide (LDH) around the CoP (CP) nanowires (NWs), supported on carbon cloth (CC), where NV-31-CP (Ni : V = 3 : 1) was found to be the optimized electrode (Fig. 5).⁴² In the case of alkaline electrolyte (1 M KOH; pH 14), NV-31-CP delivered 10 mA cm^{-2} at -55 mV versus reversible hydrogen electrode (RHE). The charge transport was examined by the EIS investigation between 1 MHz and 10 mHz at -1.15 V versus Hg/HgO (1 M NaOH), -0.4 V versus saturated calomel electrode, or -1.2 V versus Ag/AgCl (1 M KCl) electrode. The smallest semicircle of NV-31-CP in the high-frequency region confirmed a low R_{ct} (Fig. 5a). The ECM fitting exhibits one R_s (4.2Ω), two R_{ct} components of 0.7 and 2.7 Ω and two CPE components. The two R_{ct} values arise from the two interfaces, namely, the catalyst/CC and the electrode/electrolyte interface, whereas CPE appears from the surface heterogeneity at different interfaces. The self-supported electrode NV-31-CP retained its HER activity even at pH = 0 (0.5 M H_2SO_4), needing -93 mV versus RHE to reach -10 mA cm^{-2} with 0.77 mg cm^{-2} catalyst loading. NV-31-CP exhibited an R_{ct} of 1.1 and 5.7 Ω in the acidic medium (Fig. 5b). At pH 7 (0.1 M PBS), although the higher ohmic resistance and diffusion resistance of the electrolyte persist, the NV-31-CP electrode exhibits an overpotential of -311 mV versus RHE, where high solution and diffusion resistance led to the low current density. Hence, the semicircles in the Nyquist plot are also larger, fitted with a different equivalent circuit, demonstrating ten times higher R_{ct} value (Fig. 5c). The sensitivity of the EIS technique allows a dramatic change in the R_{ct} with the solution pH, which substantially impacts the electrode/electrolyte interface because of the variation in ionic mobility, diffusivity, and conductivity. Additionally, the pH of the electrolyte solution dictates the ionic diffusion, thereby influencing the charge transfer at the electrode/electrolyte interface. Conventionally, in acidic media abundant with H^+ ions, and alkaline media rich in OH^- ions, R_s and R_{ct} tend to be lower compared to that in the neutral media. However, the ohmic and diffusion resistance do not always follow a linear relation with the solution pH. This is because the intermediates formed at the electrode surface and the properties of the electrode surface itself can modify the overall resistance within the equivalent circuit.

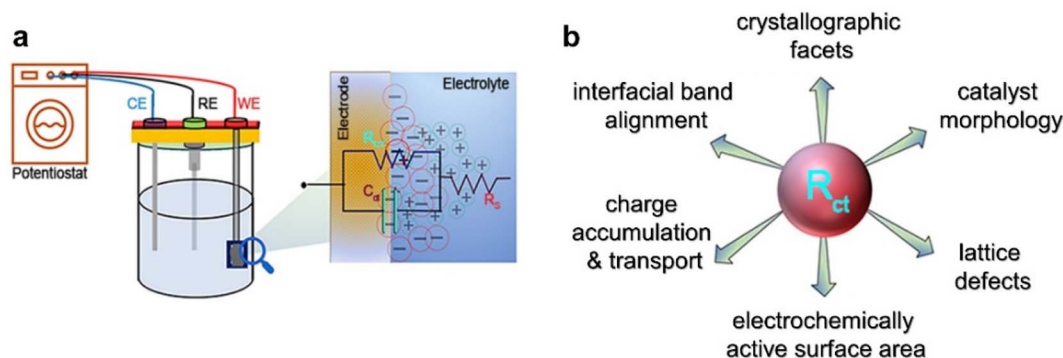


Fig. 4 (a) Measurement of impedance of the OER and HER electrocatalysts in three electrode configurations. The zoomed-in image shows the different physical parameters at the interfaces: R_s , R_{ct} and C_{dl} . (b) The parameters governing the R_{ct} of an electrocatalyst.

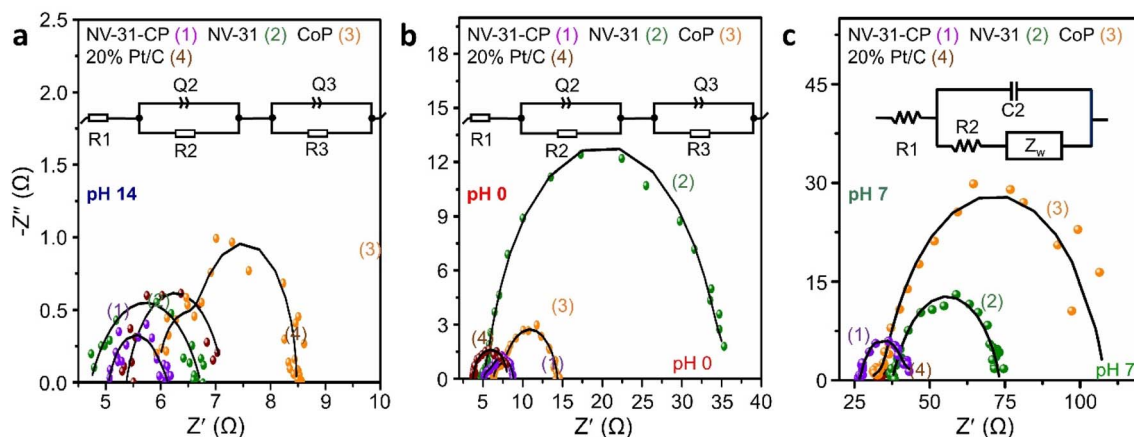


Fig. 5 Nyquist plots and corresponding ECM fitting of the NV-xy-CP heterostructure electrocatalysts in (a) 1 M KOH (pH 14), (b) 0.5 M H₂SO₄ (pH 0), and (c) 0.1 M PBS. Reprinted from ref. 42. Copyright (2022), with permission from the Royal Society of Chemistry.

There are few instances where the catalysts have reached or extrinsically bettered the benchmark limit of the precious metal-based electrocatalysts, *viz.*, Pt, RuO₂, and IrO₂.^{43,44} By employing earth-abundant elements, Ni-Co layered double hydroxide (NiCo-LDH; Ni:Co = 1:1, 1:2, 2:1) was electrodeposited on Cu wire (Cu-W) supported on Cu-mesh (Cu-m).⁴⁵ The optimized catalyst Cu-m/Cu-W/NiCo-LDH (Ni:Co = 1:1) had a current density of -100 mA cm^{-2} at a low overpotential of 139 mV, whereas 40% Pt/C required 258 mV overpotential to reach the same current density in 1 M KOH (Fig. 6a). Since the R_{ct} value is inversely proportional to the faradaic charge transfer, Cu-m/Cu-W/NiCo-LDH showed a lower R_{ct} (Fig. 6b). In 0.5 M H₂SO₄, the optimized catalysts maintained a low overpotential and R_{ct} values (Fig. 6c and d). Similarly, the cost-effective OER/HER bifunctional electrodes were fabricated by depositing Ni nanoparticles (NPs) on cellulose paper (Ni-P) by electroless plating and further electrodepositing Ni-Mo alloy (for HER) and NiFe-LDH (for OER).⁴⁶ Compared to bare Ni-P, which required 128 mV HER overpotential to reach 10 mA cm^{-2} , NiMo/Ni-P required only 32 mV (Fig. 7a). EIS measurements were made between 100 kHz and 10 mHz and maintaining an AC amplitude of 10 mV, with the working electrode biased at a DC potential of 0.1 V *vs.* RHE for HER. NiMo/Ni-P has lesser R_{ct} than Ni-P and Ni foam (Fig. 7b). The Nyquist plots were fitted with TLM to elucidate the physical significance of R_{ct} (Fig. 7c). The R_{ct} of NiMo/Ni-P was 0.75 Ω , smaller than that of the bare Ni-P electrode (1.3 Ω). In the case of OER, the NiFe-LDH/Ni-P anode displayed a distinct anodic peak at about 1.35 V (Fig. 7d). O₂ gas bubbles were not observed up to 1.45–1.47 V since the peak at about 1.3–1.4 V were from the Ni²⁺ to Ni³⁺ electro-oxidation. To avoid ambiguity from the Ni²⁺ to Ni³⁺ oxidation, 50 mA cm⁻² was chosen instead of 10 mA cm⁻². The overpotential of NiFe-LDH/Ni-P was low, merely 241 mV at 50 mA cm⁻². EIS measurements with the working electrode biased at 1.6 V *versus* RHE for OER manifested a very small semicircle for NiFe-LDH/Ni-P as compared to Ni-P and Ni-foam (Fig. 7e and f). Thus, a drop in R_{ct} from 1.6 Ω for bare Ni-P to merely 0.3 Ω for NiFe-

LDH/Ni-P implied a better charge transfer dynamics at the electrode/electrolyte interface.

Although being the best alternatives to precious metals, Ni-based HER electrocatalysts are prone to Ni-oxide formation,⁴⁶ have a relatively high affinity towards hydrogen,⁴⁷ and suffer from leaching in acidic media.⁴² Therefore, alloying Ni with other elements provides a promising avenue to achieve an active and durable catalyst.⁴⁸ A heat-up decomposition method could synthesize monodispersed Ag-Ni bimetallic heterogeneous alloy as an HER catalyst,³¹ where the material design was challenging due to the formation of different elemental phases of Ni and Ag at all temperatures.^{49,50} Ag concentration was systematically varied, and at ~ 5 at% Ag, the AgNi-5 NCs completely converted to a decahedral shape with five-fold intertwined geometry with Ni-rich faces and Ag-rich ridges and apex sites (Fig. 8a). AgNi-5 NCs demonstrated a commendable HER activity requiring $24.0 \pm 1.2 \text{ mV}$ *versus* RHE to achieve 10 mA cm^{-2} in 1 M KOH, at par with 20% Pt/C, which required $20.1 \pm 0.8 \text{ mV}$ (Fig. 8b). The Nyquist semicircle of only Ag indicates its decreased HER performance in comparison to pristine Ni (Fig. 8c). AgNi-5 showed the lowest R_{ct} of 0.75 Ω . Among other variants, the R_{ct} values were 2.05, 0.89, 1.56, 3.87 and 44.45 Ω for AgNi-1, AgNi-10, AgNi25, Ni and Ag NCs, respectively. The presence of two R_{ct} was attributed to the charge transfer in between the electrode/electrolyte interface and the Ag-Ni interface. The synergistic effect of two charge transfer processes occurs between the H-adsorbate and the catalyst surface and between Ag or Ni sites and the surrounding atoms on the surface. In fact, any lattice or tensile strain can change the electronic pathways, which can be easily detected in the EIS investigations.⁵¹

The impedance from a reaction with adsorbed intermediates at the interfaces can also be derived theoretically to correlate with the experimental data, where more than one semicircle can be obtained depending on the rate constant of each step.^{52,53} The reaction response is entangled with the inherent diffusion process, interlayer charge transport, and geometry of the

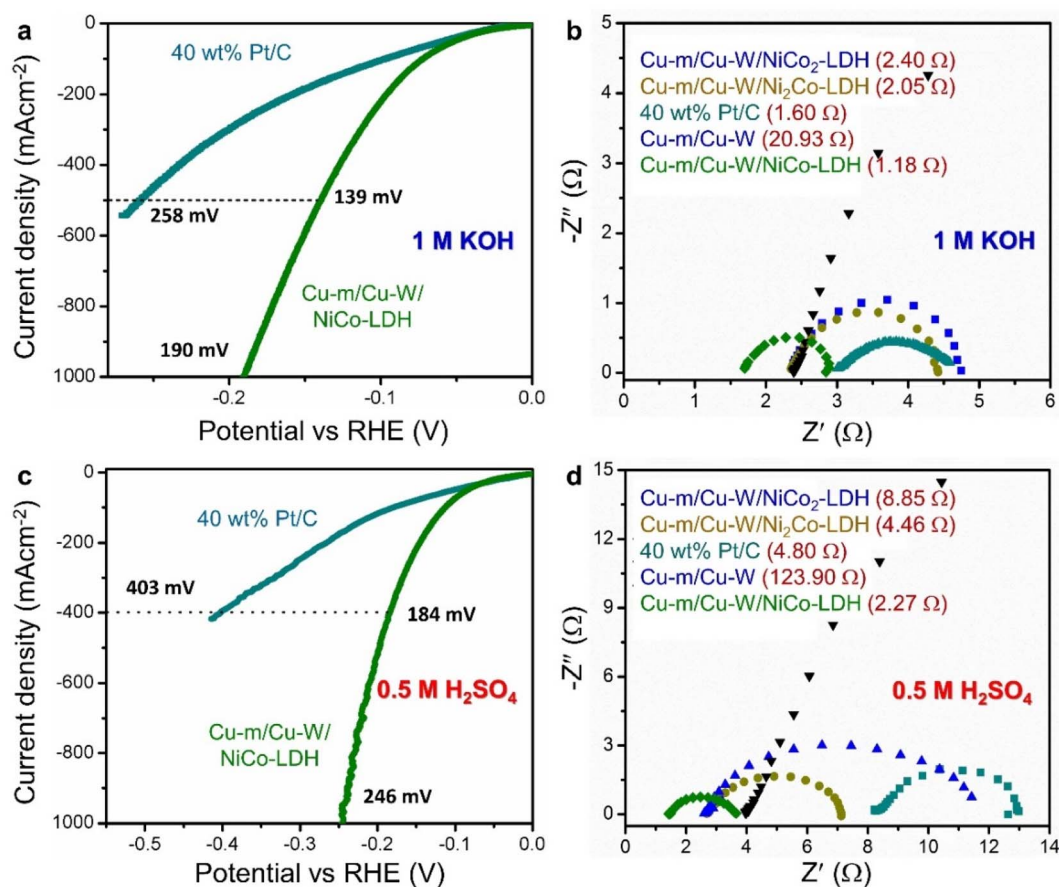


Fig. 6 HER polarization curves (iR -corrected) and the corresponding Nyquist plots in (a and b) 1 M KOH, and (c and d) 0.5 M H₂SO₄, respectively. The R_{ct} values are mentioned in the insets of panels (c) and (d). Reprinted from ref. 45. Copyright (2020), with permission from the Royal Society of Chemistry.

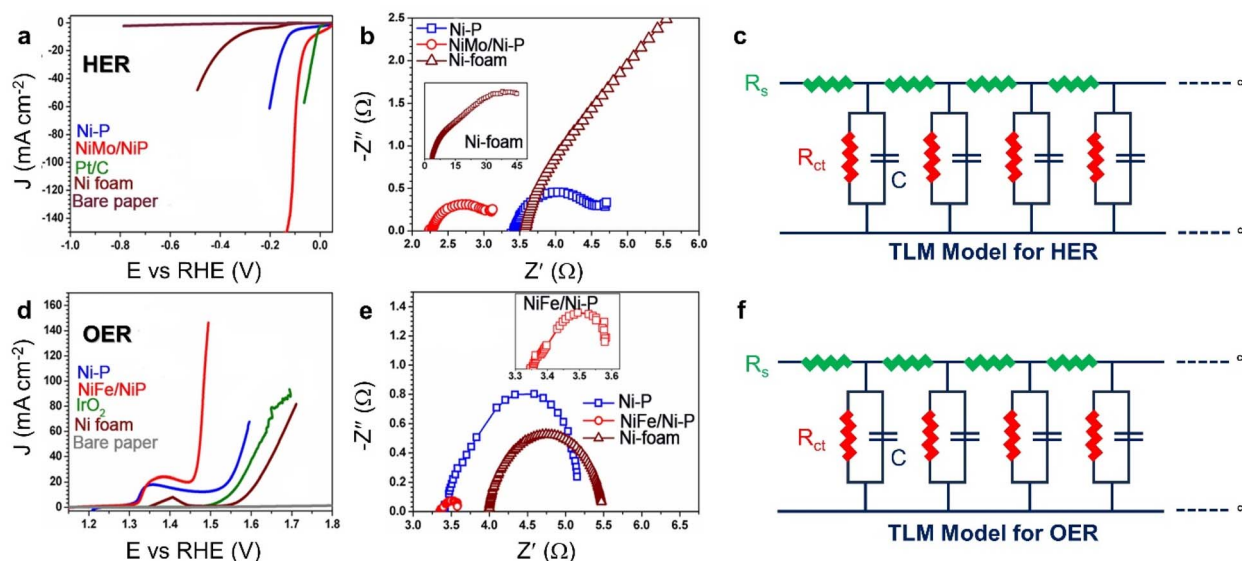


Fig. 7 LSV polarization curve (iR -corrected), Nyquist plots and the equivalent TLM of the paper-based electrodes: Ni-P, NiFe/Ni-P, and NiMo/Ni-P for (a–c) HER, and (d–f) OER, respectively. Reproduced from ref. 46. CC BY 4.0 with permission from Springer Nature.

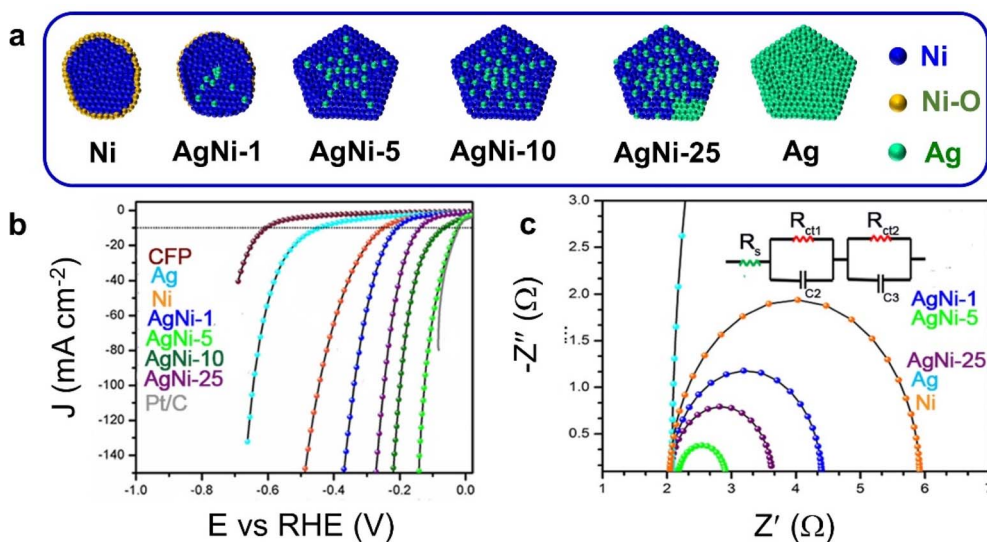


Fig. 8 (a) Illustration of the shape and site-specific composition of AgNi NCs. (b) LSV polarization plots in 1 M KOH demonstrating the electrochemical HER catalysed by AgNi NCs. (c) Nyquist plots of different AgNi NCs. Inset shows the equivalent circuit. Reproduced from ref. 31. Copyright (2020) with permission from John Wiley & Sons. Published by WILEY-VCH Verlag GmbH & Co. KGaA, Weinheim.

electrode, *e.g.*, porosity and roughness that govern the electrolyte diffusion, and the interaction of solvent molecules with the active sites. For the elucidation of the role of substrate topography in the alkaline HER activity of Ni–Mo catalyst coated on the Ni foam, the two most common ECMs, *EqCrt1* and *EqCrt2*, were used (Fig. 9a).³⁸ EIS data was collected between 0.7 Hz and -100 kHz with 10 mV AC amplitude, along with different DC bias at 200 to -400 mV *versus* RHE. The R_s and inductor (L) were associated with the electrolyte and electrical connections. In the first *EqCrt1*, the high f components were correlated with the surface geometry and the low f region was tailored by reaction kinetics. At low f , the electrolyte ions can get enough time to interact with the electrode surface. The second model was derived from the reaction kinetics and the double-layer surface (CPE_{hf,2}). The $R_{hf,2}$ indicates the R_{ct} , but low f components ($R_{lf,2}$ and CPE_{lf,2}) are associated with the changes in the adsorbed

coverage. The CPE at the low f region is interrelated with EDLC, whereas at the high f region, the CPE can be rationalized with a Schottky-type barrier. With the increment in negative potential, $R_{lf,1}$ decreased drastically, implying an increasing HER activity.

The intrinsic catalytic activity is adjudged by its turnover frequency (TOF),³⁸ and EIS is a powerful alternative tool to calculate the TOF of a catalyst.⁵⁴ Conventional TOF (TOF_{app}) is extracted with the potential-sweep measurements using the relation $TOF_{app} = J/nFC$ where, J is linear sweep voltammetry (LSV)-derived current density ($A\ cm^{-2}$), n is the number of transferred electrons per catalytic site (4 for OER), F is Faraday constant ($96\ 485\ C\ mol^{-1}$) and C represents the density of active sites ($mol\ cm^{-2}$). The OER active site density (C) is obtained by integrating the reduction peak (of OER active center) from the cyclic voltammogram (CV).⁵⁵ However, TOF_{app} suffers from the

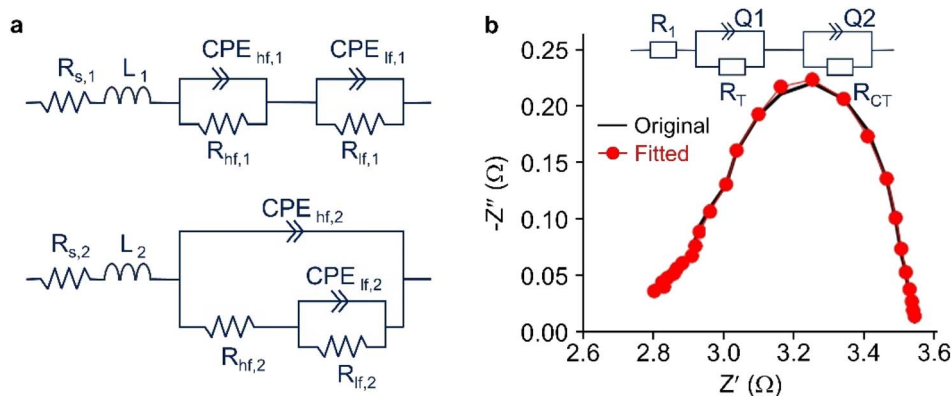


Fig. 9 (a) ECMs abbreviated *EqCrt1* and *EqCrt2* used for the fitting data of Ni–Mo alloy catalysts on different substrates in 1 M NaOH. Reproduced from ref. 38 Copyright (2019), with permission from American Chemical Society. (b) Overlay plot of original and fitted Nyquist plot at a potential 1.574 V vs. RHE for Fe/Ni-MIL-53-400. Reproduced from ref. 55 with permission from American Chemical Society.

inherent *iR*-drop associated with catalyst-conductivity and mass transport resistance. TOF can be calculated from EIS (TOF_{EIS}) at various potentials by solely gauging the catalyst–electrolyte interface. The derived electrical components from the fitted ECM can be used to calculate TOF_{EIS}, avoiding any contribution from other potential drops in the electrochemical cell: TOF_{EIS} = 1/ $n\tau$; $\tau = R_{ct} \times C_{\mu}$, where τ is time-constant (s), a combination of R_{ct} and C_{μ} (chemical capacitance). τ is related to the OER kinetics at the catalyst–electrolyte interface. In this context, the electrocatalysts based on metal–organic framework (MOF) have recently received enough attention⁵⁶ although their activities remain below those of the all-inorganic solid state systems. When Fe/Ni-MIL-53 was treated at different temperatures, the OER polarization trends did not follow that of TOF_{app} (Fig. 9b).⁵⁵ In this case, TOF_{app} and TOF_{EIS} had a gap of one order of magnitude, indicating that one can predict the maximum achievable electrocatalytic performance by evaluating the TOF_{EIS}. This sheds light on the significance of amplifying the charge-transport by nullifying the efficiency loss due to mass-transport limitations.

5.2 Carbon dioxide reduction (CRR)

In electrochemical CRR with high product selectivity, a low R_{ct} ensures fast electron transfer to CO₂ for stabilizing the CO₂^{•-} intermediate.^{57,58} Since water is the scalable source of electrons and protons, OER remains as the anodic reaction.⁵⁹ While a bulk pH close to 7 is optimal, a higher or lower local pH results in more Nernstian loss, reducing the bias used to drive the CRR kinetics at the cathode and water oxidation at the anode.⁶⁰ The distribution of molecular CO₂ versus other forms of oxidized carbon, such as H₂CO₃, HCO₃⁻, and CO₃²⁻, is strongly pH-dependent. The rate-limiting intermediate product is the CO₂ free radical (CO₂^{•-}). In a near-neutral electrolyte, under more negative bias, the pH near the cathode increases during CRR, which ultimately reduce the CO₂ concentration near the cathode. Z'' describes the dynamic process due to the electrode surface coverage by CO₂ adsorption.⁶¹ Thus, understanding the behaviour at the electrode/electrolyte interface is crucial for designing efficient CRR electrocatalysts.

Since HER is a concomitant process alongside CRR, a careful analysis of the Nyquist plots can reveal the superimposed

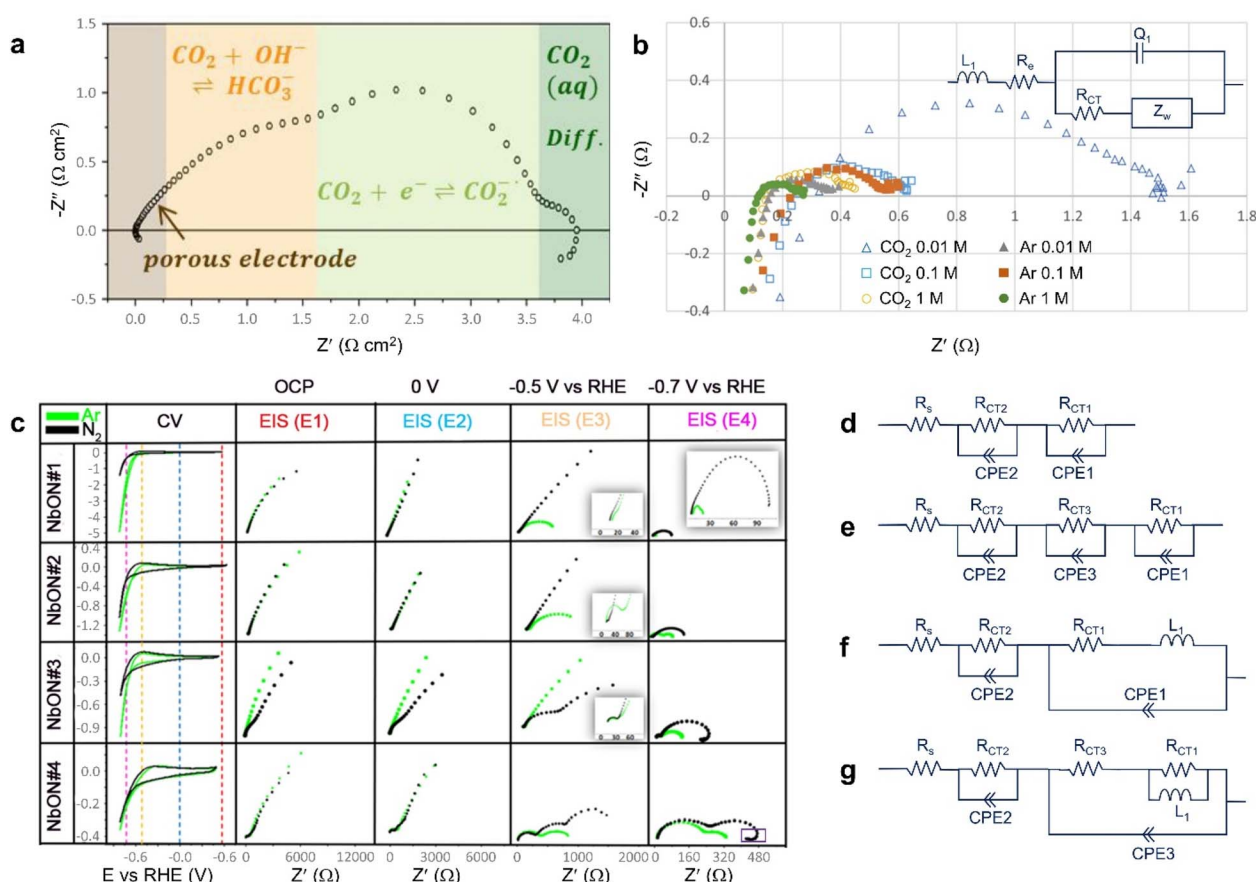


Fig. 10 Electrochemical CO₂ and N₂ reduction. (a) Identification of the multiple processes in the Nyquist plot from C-supported Sn-based gas-diffusion electrode, revealing the superimposed features, by the alteration of the CO₂ partial pressure, current density, electrolyte, and temperature. Reproduced from ref. 62. Copyright (2020), with permission from American Chemical Society. (b) Nyquist plot of the PEM electrolyser at 200 mA cm⁻², between 100 kHz and 1 Hz with a frequency ratio of 1.47 between the adjacent measurement points. Inset shows the ECM. Reproduced from ref. 63. Copyright (2023), with permission from The Japan Society of Applied Physics. (c) CV and EIS studies of NRR on NbO_xN_y thin films in Ar (green) and N₂ (black) gas. E1–E4 are equivalent to the open circuit potential, 0 V, -0.5 V, and -0.7 V versus RHE, respectively. The violet box in the last Nyquist plot highlights the arc in the positive imaginary region. (d–g) The ECMs at E4. Reproduced from ref. 68. Copyright (2022) with permission from the Elsevier.

features, where HER may dominate the CRR depending on the operating point. The C-supported Sn-based gas-diffusion electrodes were studied by altering the CO₂ partial pressure, current density, electrolyte, and temperature, where multiple processes could be identified from the Nyquist plots (Fig. 10a).⁶² During the conversion of CO₂ to formate and CO, in aqueous 1 M KOH, the spectra revealed the ionic and electronic conductivity in the porous matrix (45° line at high-frequency), the reaction of CO₂ with hydroxyl ions to form bicarbonate (in the high-frequency range), the charge transfer mechanism in the formation of CO₂^{•-} (at medium frequency), and the liquid phase diffusion of CO₂ (small arc in the low-frequency region). On the other hand, in polymer electrolyte membrane (PEM) reactors, the estimation of internal voltage distribution is quite strenuous. One of the ways to separately determine the anode and cathode voltages and the membrane ohmic loss is to set three reference electrodes and investigate the voltage in each of them (Fig. 10b).⁶³ The ohmic drop in the cell can be obtained by multiplying the resistance of the electrolyte membrane by the cell current. A higher electrolyte, and CO₂ concentration enhances the charge-carrying anions in the membrane, which also increases the ohmic drop (first semicircle shift in Fig. 10b). The series resistance was obtained from the intercept of the impedance on the real axis of the Nyquist plot, the point where the resistance in the electric double layer vanishes. However, the complexity of the CRR process did not provide any clarity between the charge transfer (at half circle) and the diffusive processes at lower frequencies.

5.3 Nitrogen reduction reaction (NRR)

The major gridlocks in electrochemical NRR are the high bond dissociation energy of N₂ triple bond and the concomitant HER, which lowers the NH₃ yield.⁶⁴ The associative/dissociative, distal/enzymatic pathways have distinct reaction intermediates in the N₂ hydrogenation arrangement. The process depends on the nature of the initial adsorption of N-radical; hence, maximizing the N₂ adsorption on the active site is vital for effective catalyst design, besides the easy release of NH₃.⁶⁵ The N₂ bond has been weakened by modulating the charge densities by heteroatom doping in a carbon matrix.⁶⁶ In general, the best electrocatalysts have a small arc at low and mid frequency regions in the Nyquist plot due to the contributions from HER and NRR.

Dynamic EIS at multiple potentials can elucidate the NRR process, *viz.*, at the open circuit potential (E1), capacitive zone (0 V *versus* RHE, E2), onset potential (−0.5 V *versus* RHE, E3), and the faradaic zone (−0.7 V *versus* RHE, E4).⁶⁷ The measurements were performed on NbO_xN_y thin films in Ar/N₂ saturated 0.1 M KOH electrolyte with an amplitude of 10 mV rms and 10 points/dec between 1 MHz and 0.1 Hz (Fig. 10c–g). DC sputtering could tune the oxygen (*x*) and nitrogen (*y*) ratios as *x* + *y* = 1.22, 1.28, 1.43, 1.52: NbON#1–4. When the potential reached E3 (under Ar), a lower *R*_{ct} was observed for NbON#1 and NbON#2, implying the inhibited HER side reaction. At the same potential, the more adsorption of species (under N₂) led to a larger semicircle with higher *C*_{dl}. NbON#2–4 has a third *R*_{ct} (under N₂),

which was absent in the Ar at E1–E3. The first charge transfer at high frequency (10²–10⁵ Hz) had lower impedance, and *Z*_W was observed only for NbNO#3–4 at E4 because of the minimal mass transport (Fig. 10c). In NbNO#3 and #4, the inductor element in the faradaic region indicates reduced coverage of the adsorbed and partially reduced N-intermediates. The two *R*_{ct}/*C*_PE combination was found to be the best fit for the data collected in Ar, and this circuit was also the best representative model for surfaces having higher N/O ratios (NbON#1 and NbON#2) in N₂ medium (Fig. 10d). For NbON#3 and NbON#4, the addition of one extra *R*_{ct}/*C*_PE component provides better data fitting (Fig. 10e). For NbON#3 and #4, under N₂, a negative curvature in the low frequency region at E4 indicates the presence of an inductor component (Fig. 10f and g). Since inductance always impacts the high frequency region, the arc in the positive imaginary region at low frequency might be an effect of the parallel integration of “negative differential capacitance” and “negative differential resistance” (Fig. 10c).⁶⁸ This also suggests ion migration in the direction of the applied DC bias.

6. Electrochemical energy storage

EIS has been extensively used to unravel the operation of energy storage systems such as batteries and supercapacitors.⁶⁹ The resistance-induced polarizations, *i.e.*, ohmic *R*_Ω, activation-charge transfer, *R*_{ct} and concentration polarization by mass transport, *R*_{mt} constrict the thermodynamically conceivable energy density of the batteries, particularly at kinetically harsher conditions of high rates and/or low temperatures.⁷⁰ These polarizations can be distinguished by varying the AC voltage or current, thereby quantifying the electronic and/or ionic conductivities of electrodes, electrolytes, interfaces, and the capacitive behavior.⁷¹ Since the batteries typically work under DC potential, the resistance is more significant, making DC bias investigations more practical and application-oriented. One of the best approaches is to couple the experimental technique and a large number of numerically produced data sets. Likewise, a wide range of electrical conductivity, electrolyte thickness (*L*), redox reaction rate constant (*k*₀) and bias potentials (*ψ*_{dc}) were altered to tally with the experimentally obtained data.⁷² The continuous electrochemical reactions at the electrode/electrolyte interfaces led to a Stern layer close to the electrode and a diffuse layer away from the electrode, controlling the *R*_{ct} and *R*_{mt}, respectively (Fig. 11a).

In most cases, the active redox electrodes consist of two semicircles in the Nyquist plot. The distance from the imaginary axis (*Z*') to the first semicircle provides the resistance of the electrode (*R*_p). The diameter of the 1st semicircle can be manipulated by varying *L* and the type of electrolyte, whereas the 2nd semicircle is the combination of both *R*_{ct} and *R*_{mt}. The reaction rate and interfacial band alignment play pivotal roles in the Stern and diffuse layer formation, which ultimately guides these two resistances. In order to identify the role of current density (*j*), the amplitudes of oscillations can be examined for the faradaic, capacitive and total current densities, *j*_{F,0}, *j*_{C,0}, and *j*_{s,0}, respectively, as functions of frequency *f* (Fig. 11b).⁷² The faradaic reactions at low frequencies (*j*_{F,0} high) and the EDL

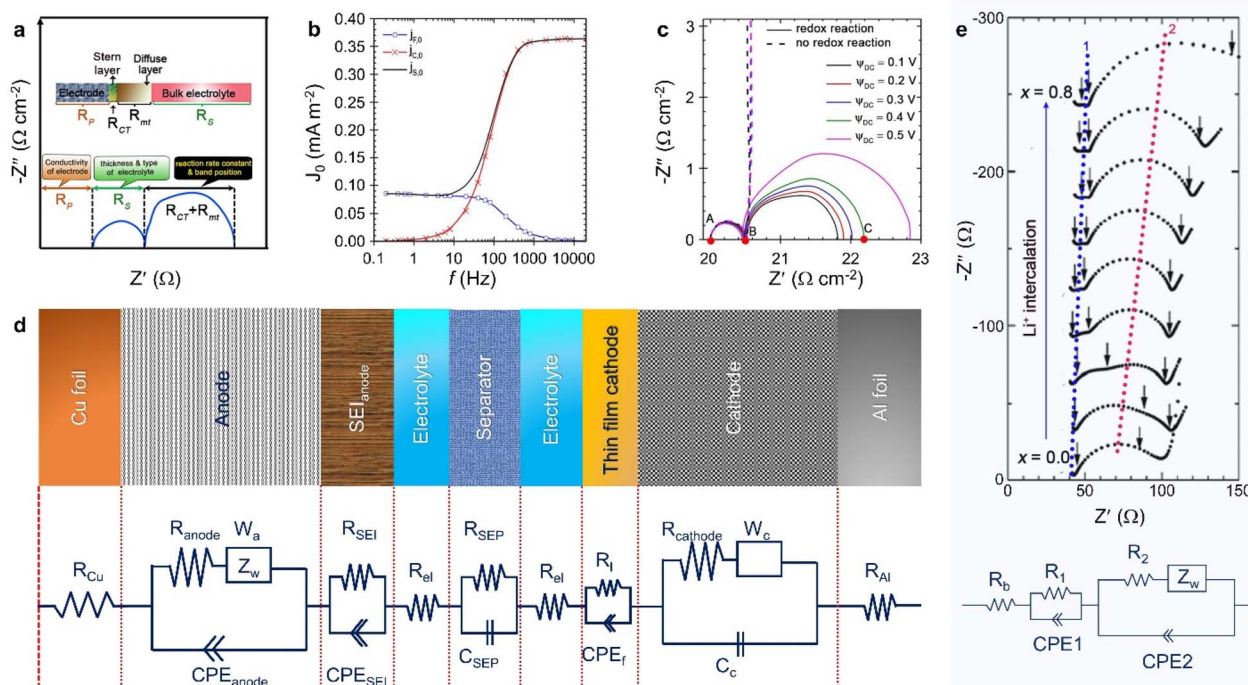


Fig. 11 EIS in Li^+ ion battery. (a) Schematic of various heterointerfaces with the MoS_2 electrode at the electrode/electrolyte junction and their resistances, (b) the current density oscillations as a function of frequency, and (c) Nyquist plots for redox (solid line) and non-redox reactions (dotted line) with bias potential ψ_{dc} of 0.1–0.6 V. Reproduced from ref. 72. Copyright (2018) with permission from American Chemical Society. (d) The individual LIB components with equivalent circuits. (e) Complex impedance plots at various compositions, x of $\text{Li}_x\text{La}_{1/3}\text{NbO}_3$, where the arrows indicate the data at 5000, 150, and 0.5 Hz, along with the equivalent circuit. Reprinted from ref. 77 with permission from American Chemical Society.

formation at high frequencies ($j_{c,0}$ high) significantly contribute to the impedance. Apart from the current density, for understanding the role of applied DC potential (ψ_{dc}) on the Nyquist plot, the potential was varied in the range of 0.1–0.6 V. Two semicircles in the case of redox-active reaction ($k_0 \neq 0$) and only one semicircle, along with a nearly vertical line in the case of redox-inactive reaction ($k_0 = 0$), were observed (Fig. 11c). Both the semicircles (AB) overlapped with each other at high frequency, where the interaction of the first semicircle with the Z' axis (A point) and its diameter is bias-independent. The A point (R_p) and the diameter of the 1st semicircle (R_s) are the intrinsic properties of the electrode and bulk electrolyte, respectively, independent of the applied bias and the type of redox reactions. In the case of redox-inactive reactions, the observed vertical line, due to the diffusion of ions at the electrode surface, is nearly independent of ψ_{dc} , where the slope of the line helps to identify whether the charging process is controlled by the double-layer formation (large gradient) or limited by ion diffusion (small slope).¹³

6.1 Lithium-ion battery

In lithium-ion batteries (LIBs), EIS is generally explained by an ECM to correlate the different components. The most common approach is to choose an ECM according to the shape of the experimentally obtained impedance curve, followed by complex nonlinear square (CNLS) fitting. A conventional LIB consists of

electrodes, liquid/gel electrolyte, separator and insulating layers including the solid-electrolyte interphase (SEI) formed during charge–discharge cycling. Fig. 11d shows the corresponding circuit model made of copper foil resistance (R), SEI, capacitance (C), and Warburg constant (W).^{73,74} In general, two semicircles are used in order to distinguish the partial desolvation reaction of Li^+ ions and their adsorption and diffusion on the electrode surface.⁷⁴ EIS aids in monitoring the formation of the passivation layer, the rate-determining Li^+ diffusion in the solid state, and the investigation of charge transfer at various stages of the electrode–electrolyte interfaces. This technique helps in understanding the Li^+ intercalation and de-intercalation processes that occur in transition metal oxides.⁷⁵ Cell degradation can be captured with the variation of the semicircle positions, shape alteration (mid frequency region) as well as the slope variation in the low frequency region. These are directly correlated with the loss of the active material, Li inventory itself, electrolyte degradation with time, and SEI growth.⁷⁶ As the LIBs age, there is a noticeable shift towards higher frequencies in both the high and intermediate frequency regions of the semicircle as well as in the Warburg diffusion component. This shift is indicative of the progressive degradation of the battery. The dendrite growth and micropore clogging within the electrodes contribute to an increase in cell resistance, which impedes the ion diffusion and consequently restricts the interfacial charge transfer.

The Nyquist plots have been used to monitor the Li^+ insertion and de-insertion kinetics in $\text{Li}_x\text{La}_{1/3}\text{NbO}_3$ as a function of x , where $0 < x < 0.6$ (Fig. 11e).⁷⁷ The results were modelled by two semicircles, where, R_b is the bulk resistance of the electrolyte, and R_i and CPE_i belong to the semicircle i ($i = 1$ or 2). The occurrence of two semicircles was explained by the ‘adatom model’, where the adatom migrates to an insertion site on the surface and the adsorbed ions are fully incorporated into the electrode.⁷⁸ Semicircle-1 corresponds to the adatom migration for ion insertion, and semicircle-2 is for the full incorporation of the adsorbed ions within the electrode. Based on the adatom model, the elemental reactions for semicircle-1 were assigned as a correlative reaction of lithium adsorption, desolvation, and electron-transfer reactions, and semicircle-2 was assigned to lithium insertion. During lithiation, semicircle-1 at higher frequency nearly disappeared at the cost of the lower frequency semicircle-2. However, due to the inherent drawbacks of ECMs for an in-depth understanding of the impedance, numerical simulations are often used by conventional physicochemical parameters and phase-dependent drift-diffusion.⁷⁹

6.2 Li–O₂ battery

In Li–O₂ batteries, oxygen reduction reaction (ORR) and OER are two complementary processes during discharge and charging, respectively.⁸⁰ Li_2O_2 is the main discharge product that is insulating and insoluble in nature, resulting in the increment of the required potential and consequently

decreasing the cyclability of the Li–O₂ battery.^{81,82} The Li–O₂ discharge process was successfully demonstrated by EIS with different cathodes, where the internal resistance resulted in the overpotential during discharge and controlled by the charge transport through the deposited Li_2O_2 at the cathode.⁸³ The discharge of Li–O₂ is governed by the interfacial phenomena, EDLC, and ORR capacitance. When the cathode was made of super carbon with 30% NiOCoO, three main ORR steps could be unravelled.⁸³ Firstly, in the presence of O_2 , the interfacial phenomena gave rise to two arcs in the Nyquist plot, where the two resistance components are parallel to the two capacitors, and in the absence of O_2 , another equivalent arc was observed. Secondly, Li^+ adsorption gave rise to a series of R, C circuit and related to C_{dl} at an intermediate frequency.⁸⁴ The third phenomenon was related to ORR capacitance, which appeared in the low frequency range (<10 mHz). To account for the ORR capacitance, the chemical capacitance (C_{μ}) was modelled with the EDLC.

6.3 Zn–air/Zn–O₂ battery

The basic configuration of zinc–air batteries (ZABs) consists of a catalyst loaded air electrode (cathode), a membrane separator, an alkaline electrolyte and a zinc anode.^{85,86} During discharge, the air-electrode undergoes ORR to form OH^- , collecting O_2 from the air, whereas the zinc electrode undergoes oxidation to form soluble zincate ions, *i.e.*, $\text{Zn}(\text{OH})_4^{2-}$ in the electrolyte. The ZAB performance could be enhanced by introducing measured defects

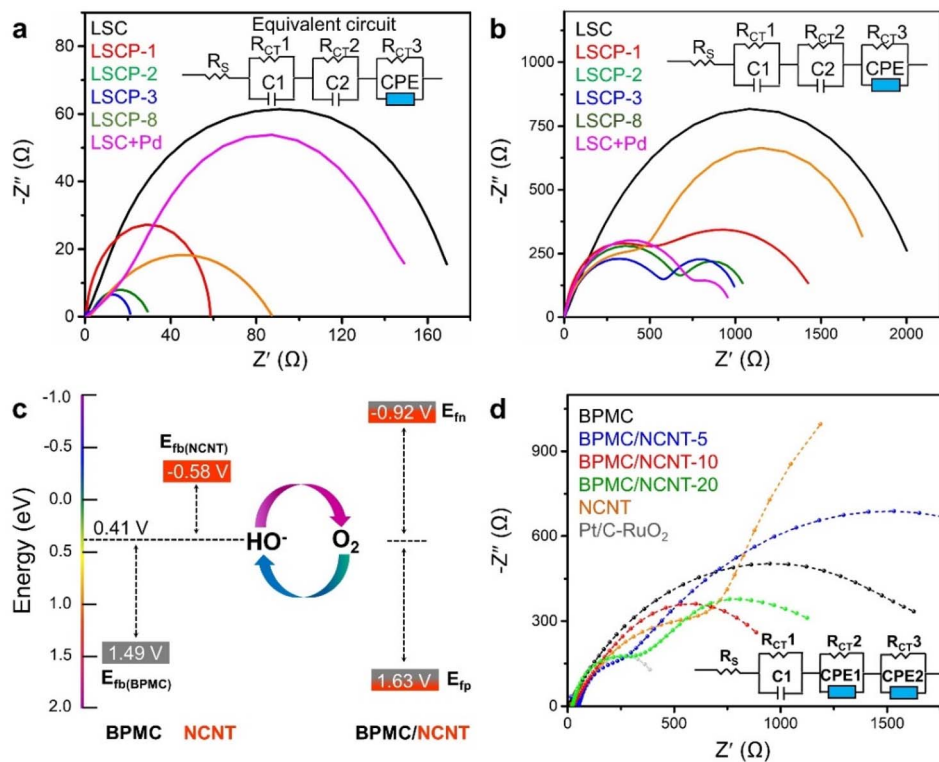


Fig. 12 Nyquist plots of LSC, LSCP and LSC + Pd electrocatalysts during (a) OER and (b) ORR polarizations at 1.6 and 0.6 V versus RHE, respectively. Reproduced from ref. 87. Copyright (2020), with permission from American Chemical Society. (c) Schematic of E_{fb} alignment of BPMC, NCNT and BPMC/NCNT-10 with respect to standard O_2 electrolysis potential in alkaline medium, and (d) Nyquist plots under ORR conditions. Reproduced from ref. 39. Copyright (2020), with permission from the Royal Society of Chemistry.

in the bifunctional catalyst. Pd⁴⁺ was doped at the Co-site of La_{0.7}Sr_{0.3}CoO_{3-δ} to introduce lattice defects due to the strain between the lesser doped grains and the more Pd-doped grain boundaries.⁸⁷ A multitude of Pd/Co molar ratios were studied, *viz.*, La_{0.68}Sr_{0.3}Co_{0.95}O_{2.73} (LSC, Pd/Co = 0), La_{0.7}Sr_{0.3}Co_{0.96}Pd_{0.01}O_{2.88} (LSCP-1, Pd/Co = 0.01), La_{0.7}Sr_{0.3}Co_{0.94}Pd_{0.02}O_{2.85} (LSCP-2, Pd/Co = 0.03), La_{0.7}Sr_{0.3}Co_{0.9}Pd_{0.03}O_{2.85} (LSCP-3, Pd/Co = 0.05), La_{0.7}Sr_{0.3}Co_{0.85}Pd_{0.07}O_{2.88} (LSCP-8, Pd/Co = 0.1), and LSC + Pd (physical mixture of the undoped perovskite oxide with Pd). Fig. 12a presents the Nyquist plots corresponding to OER at 1.6 V *versus* RHE with an AC frequency range from 10 mHz to 1 MHz. With increasing Pd concentration, R_{ct} decreased up to LSCP-3 (Pd/Co = 0.05), after which R_{ct} gradually increased. LSCP-3 has higher C_{dl} , which was in good agreement with the maximum number of surface-active sites in LSCP-3. In Fig. 12b, R_s represents the electrolyte resistance, R_{ct1} , R_{ct2} and R_{ct3} represent the charge transfer resistances, and C_1 & C_2 are from C_{dl} . For the ORR process, LSC + Pd has the least R_{ct} due to the presence of ORR-active Pd in the mixture. However, the structural transformation of the perovskite oxide due to optimum Pd-incorporation at the grain boundary for LSCP-3 exhibits the lowest OER + ORR overpotential of 0.91 V in alkaline electrolyte with a current density of 10 and -1 mA cm⁻² for OER and ORR, respectively, having a discharge energy density of 851 mW h g_{Zn}⁻¹ with stable performance for 60 cycles of 1 h duration per cycle at 10 mA cm⁻².

The OER/ORR bifunctional activity can be greatly enhanced by combining N-doped carbon nanotubes (CNTs) with a metal oxide catalyst. Engineering the p-type BaPrMn_{1.75}Co_{0.25}O_{5+δ}, BPMC nanosheets with n-type N-doped CNTs (NCNTs) induces a charge transfer from BPMC to NCNT, which enhanced the bifunctional activity.³⁹ Mott-Schottky measurements with different weight% of NCNTs exhibited a p-n heterojunction where the charge transfer shifts the flat band energy (E_{fb}) of BPMC and NCNTs towards more positive and negative values, as compared to their bare counterparts, attributed to the n- and p-type E_{fb} values of -1.06 (E_{fn}) and 1.79 V (E_{fp}), respectively (Fig. 12c). A higher charge density on NCNTs shifted the E_{fn} towards more negative values, *i.e.*, higher energy and depletion in charge density in BPMC, facilitated the electrochemical oxidation reaction. Thus, an optimum E_{fb} was necessary to facilitate both the reactions. During OER, BPMC/NCNT-20 performed the best with an overpotential of 390 mV at 10 mA cm⁻², whereas BPMC/NCNT-10 served as the best performing ORR catalyst with 366 mV overpotential at -1 mA cm⁻². The estimated R_{ct} from the Nyquist plot for BPMC/NCNT-5, BPMC/NCNT-10, BPMC/NCNT-20, BPMC and NCNTs was 2.84, 1.55, 1.56, 2.71 and 3.45 kΩ, respectively (Fig. 12d). Although BPMC/NCNT-20 exhibited weaker ORR performance, it had almost similar R_{ct} with respect to BPMC/NCNT-10. Higher concentrations of NCNT in BPMC/NCNT-20 drastically reduced the overall resistance of the catalyst, which played a pivotal role in maintaining an almost equivalent R_{ct} value to that of BPMC/NCNT-10.

6.4 Photo-rechargeable battery

Solar cells are typically merged with rechargeable batteries to address the power requirements, but using two separate devices

introduces more complexity, cost and ohmic transport losses. The integrated solar rechargeable battery is proposed to resolve the issues where photo-charge generation and storage coincide to reduce the ohmic losses and for increasing the gravimetric energy density. Photo-rechargeable single storage devices, such as solar light-driven aqueous zinc ion batteries,⁸⁸ redox flow batteries,⁸⁹ lithium-air batteries,⁹⁰ LIBs,⁹¹ and electrochemical capacitors,⁹² can be recharged directly in the presence of light. However, they suffer from low capacities, poor cycling stabilities, and photon-to-charge storage conversion efficiency. These shortcomings are closely linked to the electronic conductivity and structural stability of the electrode material, thus exhibiting correlation with the impedance at the electrode/electrolyte interface. Interestingly, under photo-illumination, the impedance can be reduced, and the specific capacity enhanced, highlighting the light-induced improvements in the battery performance. For a representative V₂O₅ nanofiber-based photo-rechargeable LIB with a photoconversion efficiency of 2.6% under 455 nm laser illumination, the photogenerated electrons are transported from the conduction band of V₂O₅ to the CF current collector during charging, hole transport occurs from P3HT, and the electrons flow through the external circuit to the Zn anode.⁹¹ The current density and Li⁺ diffusion coefficient was enhanced by 65 and 64.4% in the presence of light for the cathodic and anodic reactions, respectively, at ~3.11 V/~3.53 V. The Nyquist plots were measured from 10 mHz to 100 kHz with a voltage amplitude of 10 mV. R_{ct} decreased from 32 to 14 Ω under illumination. The carrier mobility increased in the presence of light, resulting in a higher electrical conductivity of the photocathode, which was evident from the lower R_{ct} .

7. Conclusions & outlook

We have studied the hetero-interfacial electronic interactions that modulate the charge transfer in the electrochemical energy systems. Starting from the EIS models, few selective examples in water electrolysis, CRR, and NRR for electrochemical energy conversion were highlighted, followed by the energy storage systems of Li⁺ ion/O₂, Zn²⁺ air/O₂ and photo-rechargeable batteries. Minimizing the R_{ct} at the electrode/electrolyte interface is essential for enhancing the efficiency of diverse electrochemical devices. Achieving a lower R_{ct} involves several strategies, including ensuring an unobstructed electron pathway in an electronically conductive electrodes, achieving the near-perfect alignment of the Fermi energy levels to facilitate smooth carrier transport and implementing electrode architectures with low tortuosity, *i.e.*, high porosity. Such architectures promote efficient charge transport kinetics in metal-ion batteries, thereby contributing to the improved device performance and overall efficiency. Since most of the traditional electrochemical setups cannot apprehend the faradaic and non-faradaic current components, impedance analysis has become a commanding tool. The choice of a modelling circuit at the electrode/electrolyte interface depends on the specific electrochemical reaction under consideration. Broadly categorizing the electrochemical reactions such as HER, OER, ORR, CRR, and NRR, the EIS response typically exhibits a small semicircle

at high frequency along with a larger semicircle in the low frequency region. Occasionally, the small high-frequency semicircle merges with the larger one. In the case of electrochemical storage systems such as batteries, an additional slope after the second semicircle at the low-frequency region is observed, indicative of ion diffusion within the electrode material. In particular cases where the electrode material is highly porous, TLM is also considered.

The other eye-catching feature is to cross-examine an electrochemical system over a range of frequencies, thus permitting the operando investigations. In case of operando or *in situ* EIS, keeping the AC perturbation fixed at 5 or 10 mV and the current fixed at a specific value under different potential bias, the EIS experiments were carried out (Fig. 13a). One can obtain the 3D Bode and Nyquist plots, where the variation of the curve is monitored based on the two parameters, the conventional frequencies (mHz to MHz) and the applied potential (Fig. 13b and c). This inspection provides the real-time SEI layer information, which is difficult to probe in other electron beam-irradiated *in situ* techniques, which can damage the interfacial double layer.⁹³

The electrochemical reactions in a battery involve time-dependent potential variation with the charge/discharge steps, which also alter the electrode potentials.⁹⁴ Operando impedance investigations can reveal the suitability of new anode materials and monitor the charge/discharge induced changes of the electrodes and the reaction stage with applied potential.⁹⁵ The charge transfer processes can have diverse degree of responses to the input frequencies as well as the potential. Under the operating conditions, the varying crystallinity and

lattice structure of different electrocatalysts and solvation structure of the ions can also alter the catalytic activity and battery performance.^{96–98} The *in situ* EIS methods can elucidate the temporal evolution of R_{ct} at multiple heterointerfaces during the real-time surface reconstruction of amorphous or semicrystalline catalysts under continuous operation. Moreover, the resistance to the transient electron-hole transport across the interfaces of photovoltaic and optoelectronic devices can be understood by constructing the most appropriate ECM.^{99,100} More sophisticated and operando EIS techniques are needed to match the femtosecond or picosecond dynamics of photogenerated charge carriers.¹⁰¹ EIS has also been successful in probing the real-time interactions of nanoparticles with soft matter by a technique called resonance enhanced surface impedance (RESI) spectroscopy.¹⁰² RESI has very good prospects in biological systems and can be extended to heterogeneous catalysis and photocatalysis.^{103,104}

As discussed earlier, data interpretation based on a particular electrical ECM is the most challenging part of EIS investigation since the same impedance data can be fitted with different ECMs, besides the subjectivity of human analysis.¹⁰⁵ Although coupling the DFRT/DRT model with the ECM might be beneficial, DFRT models have issues like complexity in mathematical modelling and meagre handling with the system dominated by ion diffusion. In this context, machine learning (ML) can be used to recognize the right circuit model by employing large EIS datasets to corroborate the chemical and physical insights obtained from other characterization tools. An ML-based approach can track and learn from the wide range of battery systems to adjudge the predicted behaviour of the cells,

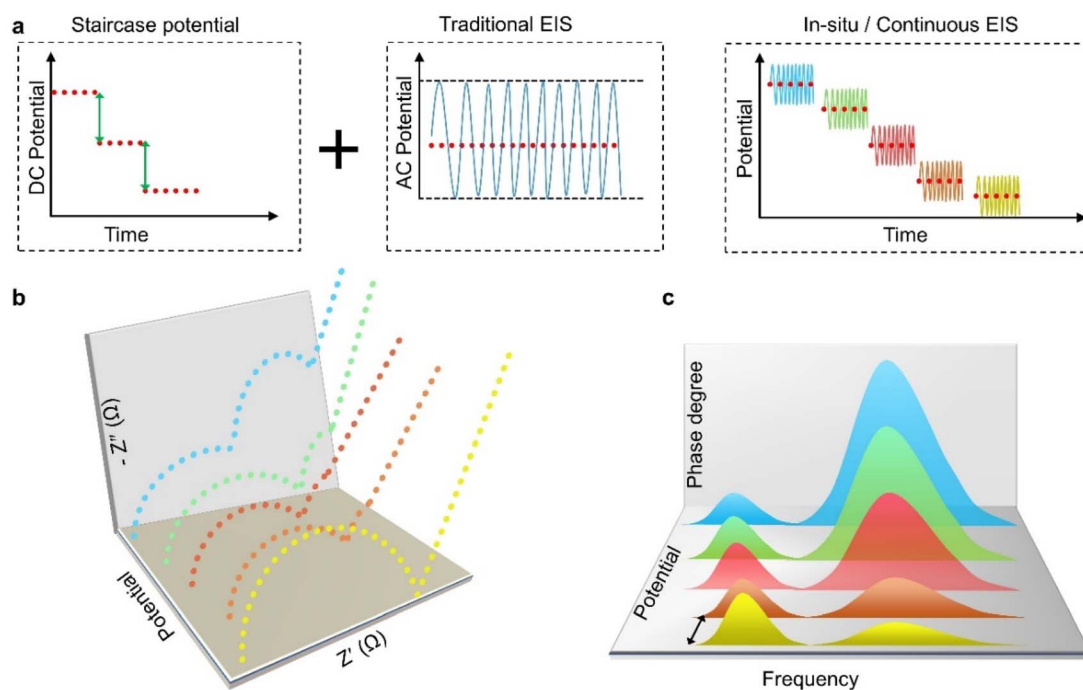


Fig. 13 (a) Integration of the DC staircase potential with the traditional EIS measurement for *in situ*/continuous EIS measurement. Potential-dependent (b) Nyquist plot and (c) Bode plot.

state-of-health, state-of-charge, and degradation behavior.¹⁰⁶ While ML needs reliable large EIS datasets, its inherent black-box nature makes it difficult to affirm and generalize the obtained models.¹⁰⁶ Support vector machine (SVM) has been proposed to analyse the raw EIS data and the corresponding ECMs that can be collected from the literature.¹⁰⁵ The SVM data needs to be compared with other ML algorithms to provide the best possible comprehensive database. The widespread implementation of ML in EIS analysis will create a paradigm shift for the automated fitting of the measured data to the appropriate physical models, thereby minimizing the human error in making first guesses.¹⁰⁷ A user-friendly database can be developed, for example, the performance of LIBs can be evaluated from a collection of ~100 000 impedance spectra from Li⁺-ion cells, maintaining the unreliability of the fitting below ~1% of the entire dataset.¹⁰⁷ These interpretations should be based on the proposed (or feasible) reaction mechanisms, followed by physical consideration and regression of the models.

Although the EIS data is elucidated by covering an extensive frequency range (mHz to MHz), conventional Nyquist impedance data does not mark the frequency points in the impedance plot. Translating the Nyquist to the Bode plot in terms of frequency & phase angle can be helpful in providing insight regarding the electrochemical and photoelectrochemical reactions.¹⁰⁸ If we consider the non-metals, mostly the heteroatom-doped carbon electrocatalysts, the compositional variation can be elucidated by EIS.^{103,109} Graphene dots are vastly different from carbon dots, where the latter contain an assembly of aromatic moieties inside a carbon envelope.¹¹⁰ The subtle nuances of the varying carbon dot compositions can be monitored if EIS measurements can confirm the marginal changes in the impedance parameters.¹¹¹ CNTs comprise a large fraction of the literature, which has generated immense interest in nanochannel chemistry and the confined catalytic mechanisms.^{112,113} The variation in nanochannel or CNT diameter with respect to the bulk electrolyte has a profound impact on the overall impedance of the system. The changes in the narrow channels from micro- to nanometers affects the viscous shear at the walls of the channels that suppresses the electro-osmotic instability, providing additional AC signals.¹¹⁴ The impedance of a deformed semicircular arc of a nanochannel has complex AC impedance, a characteristic dependent on the surface-conductivity, wherein low AC voltages are needed to extract the surface charge density.¹¹⁵

EIS also has far-reaching implications in electrophysiology, where the need of the hour is to affirmatively determine the compositional changes of the 'live' cells in order to revolutionize healthcare systems.^{112,116} Be it coupled to a Raman spectrometer or any other *in situ* techniques, each confocal microscope setup conducting these experiments is different depending on the laboratory conditions. In this technique, a 'comparatively weaker' signal is detected by a microelectrode, and an amplifier transmits the signal through an oscilloscope and a computer. The temporal evolution of the membrane potential is of primary interest, where the microelectrode has to be stabilized both for *in vitro* and *in vivo* recordings. The major point of contention is the extent to which the impedance of the

microelectrode impacts upon the spikes of the compositional changes of the cellular material as opposed to the background noise. In fact, EIS has been employed to detect and systematically monitor the extracellular signals with ~100 k Ω microelectrodes having unmodified high impedance ~1 M Ω .¹¹⁷ With the advancement in science, it is pertinent to measure the impedance signal of a single neuron with a high signal-to-noise ratio. The overall emphasis should be on improving the sensitivity of the EIS technique to record minor changes in the AC signals without any ambiguity in detection and analysis.

Conflicts of interest

There are no conflicts to declare.

Acknowledgements

K. P. thanks Science and Engineering Board (SERB) and S. M. thanks Council of Scientific and Industrial Research (CSIR), Govt. of India, for their fellowships. S. B. thanks the financial support from SERB under Sanction No. CRG/2020/000084 and STR/2021/000001.

Notes and references

- W. Li, J. Liu and D. Zhao, *Nat. Rev. Mater.*, 2016, **1**, 1–17.
- R. Majeed, S. Parvin, Q. A. Islam, A. Kumar, B. Debnath, S. Mondal, S. Bhattacharjee, S. Das, A. Kumar and S. Bhattacharyya, *Chem. Rec.*, 2022, **22**, e202200070.
- Y. P. Zhu, C. Guo, Y. Zheng and S. Z. Qiao, *Acc. Chem. Res.*, 2017, **50**, 915–923.
- Y. Y. Birdja, E. Pérez-Gallent, M. C. Figueiredo, A. J. Göttle, F. Calle-Vallejo and M. T. M. Koper, *Nat. Energy*, 2019, **4**, 732–745.
- L. R. L. Ting, R. García-Muelas, A. J. Martín, F. L. P. Veenstra, S. T. J. Chen, Y. Peng, E. Y. X. Per, S. Pablo-García, N. López, J. Pérez-Ramírez and B. S. Yeo, *Angew. Chem., Int. Ed.*, 2020, **59**, 21072–21079.
- I. Čorić, B. Q. Mercado, E. Bill, D. J. Vinyard and P. L. Holland, *Nature*, 2015, **526**, 96–99.
- X. Yang, J. Nash, J. Anibal, M. Dunwell, S. Kattel, E. Stavitski, K. Attenkofer, J. G. Chen, Y. Yan and B. Xu, *J. Am. Chem. Soc.*, 2018, **140**, 13387–13391.
- Q. Pang, D. Kundu, M. Cuisinier and L. F. Nazar, *Nat. Commun.*, 2014, **5**, 4759.
- G. Liu, N. Li, Y. Zhao, M. Wang, R. Yao, F. Zhao, Y. Wu and J. Li, *ACS Sustainable Chem. Eng.*, 2019, **7**, 11377–11385.
- B.-Y. Chang and S.-M. Park, *Annu. Rev. Anal. Chem.*, 2010, **3**, 207–229.
- A. Kumar, D. K. Chaudhary, S. Parvin and S. Bhattacharyya, *J. Mater. Chem. A*, 2018, **6**, 18948–18959.
- S. Anantharaj and S. Noda, *ChemElectroChem*, 2020, **7**, 2297–2308.
- B. A. Mei, O. Munteshari, J. Lau, B. Dunn and L. Pilon, *J. Phys. Chem. C*, 2018, **122**, 194–206.
- Z. Tang, Q.-A. Huang, Y.-J. Wang, F. Zhang, W. Li, A. Li, L. Zhang and J. Zhang, *J. Power Sources*, 2020, **468**, 228361.

- 15 A. R. C. Bredar, A. L. Chown, A. R. Burton and B. H. Farnum, *ACS Appl. Energy Mater.*, 2020, **3**, 66–98.
- 16 V. Vivier and M. E. Orazem, *Chem. Rev.*, 2022, **122**, 11131–11168.
- 17 A. Oz, K. Singh, D. Gelman, V. Thangadurai and V. Tsur, *J. Phys. Chem. C*, 2018, **122**, 15097–15107.
- 18 M. Oldenburger, B. Bedürftig, A. Gruhle and E. Richter, *J. Energy Storage*, 2017, **14**, 16–21.
- 19 T. S. Drvarič, J. Bobnar, A. R. Sinigoj, I. Humar and M. Gabersček, *J. Phys. Chem. C*, 2019, **123**, 27997–28007.
- 20 M. Schalenbach, Y. E. Durmus, H. Tempel, H. Kungl and R. A. Eichel, *J. Phys. Chem. C*, 2021, **125**, 27465–27471.
- 21 S. Hershkovitz, S. Tomer, S. Baltianski and Y. Tsur, *ECS Trans.*, 2010, **33**, 67.
- 22 S. Baltianski and Y. Tsur, *J. Electroceramics*, 2003, **10**, 89–94.
- 23 C. G. Avioz, D. Gelman and Y. Tsur, *J. Phys. Chem. C*, 2021, **125**, 11867–11874.
- 24 A. Oz, D. Gelman, E. Goren, N. Shomrat, S. Baltianski and Y. Tsur, *J. Power Sources*, 2017, **355**, 74–82.
- 25 A. Borenstein, S. Hershkovitz, A. Oz, S. Luski, Y. Tsur and D. Aurbach, *J. Phys. Chem. C*, 2015, **119**, 12165–12173.
- 26 J. Wilson, W. Kobsiriphat, R. Mendoza, H.-Y. Chen, T. Hines, J. Hiller, D. Miller, K. Thornton, P. Voorhees, S. B. Adler, D. R. Mumm and S. Barnett, *ECS Trans.*, 2007, **7**, 1879–1887.
- 27 S. Wang, J. Zhang, O. Gharbi, V. Vivier, M. Gao and M. E. Orazem, *Nat. Rev. Methods Primers*, 2021, **1**, 41.
- 28 R. Majee, S. Chakraborty, H. G. Salunke and S. Bhattacharyya, *ACS Appl. Energy Mater.*, 2018, **1**, 3342–3350.
- 29 S. Mondal, R. Majee, Q. A. Islam and S. Bhattacharyya, *ChemElectroChem*, 2020, **7**, 5005–5012.
- 30 D. Cao, H. Xu and D. Cheng, *Adv. Energy Mater.*, 2020, **10**, 1903038.
- 31 R. Majee, A. Kumar, T. Das, S. Chakraborty and S. Bhattacharyya, *Angew. Chem., Int. Ed.*, 2020, **59**, 2881–2889.
- 32 L. Zhang, L. Chen, X. Zhou and Z. Liu, *Sci. Rep.*, 2015, **5**, 18263.
- 33 R. Majee, Q. A. Islam, S. Mondal and S. Bhattacharyya, *Chem. Sci.*, 2020, **11**, 10180–10189.
- 34 Q. A. Islam, R. Majee and S. Bhattacharyya, *J. Mater. Chem. A*, 2019, **7**, 19453–19464.
- 35 Q. Ma, J. Young, S. Basuray, G. Cheng, J. Gao, N. Yao and W. Zhang, *Nano Today*, 2022, **45**, 101538.
- 36 S. J. Kim, J. Y. Koo, T. Mun, M. Choi and W. Lee, *J. Mater. Chem. A*, 2020, **8**, 23313–23322.
- 37 J. Yang, Q. Shao, B. Huang, M. Sun and X. Huang, *iScience*, 2019, **11**, 492–504.
- 38 Ī. B. Pehlivan, M. A. Arvizu, Z. Qiu, G. A. Niklasson and T. Edvinsson, *J. Phys. Chem. C*, 2019, **123**, 23890–23897.
- 39 R. Majee, S. Mondal and S. Bhattacharyya, *Chem. Commun.*, 2020, **56**, 8277–8280.
- 40 Q. Xu, J. Zhang, H. Zhang, L. Zhang, L. Chen, Y. Hu, H. Jiang and C. Li, *Energy Environ. Sci.*, 2021, **14**, 5228–5259.
- 41 A. Kumar and S. Bhattacharyya, *ACS Appl. Mater. Interfaces*, 2017, **9**, 41906–41915.
- 42 M. Maji, N. Dihingia, S. Dutta, S. Parvin, S. K. Pati and S. Bhattacharyya, *J. Mater. Chem. A*, 2022, **10**, 24927–24937.
- 43 F. Li, G.-F. Han, H.-J. Noh, J.-P. Jeon, I. Ahmad, S. Chen, C. Yang, Y. Bu, Z. Fu, Y. Lu and J.-B. Baek, *Nat. Commun.*, 2019, **10**, 4060.
- 44 J. Mahmood, M. A. R. Anjum, S. Shin, I. Ahmad, H. Noh, S. Kim, H. Y. Jeong, J. S. Lee and J. Baek, *Adv. Mater.*, 2018, **30**, 1805606.
- 45 S. Parvin, A. Kumar, A. Ghosh and S. Bhattacharyya, *Chem. Sci.*, 2020, **11**, 3893–3902.
- 46 A. Sahasrabudhe, H. Dixit, R. Majee and S. Bhattacharyya, *Nat. Commun.*, 2018, **9**, 2014.
- 47 S. Parvin, V. Hazra, A. G. Francis, S. K. Pati and S. Bhattacharyya, *Inorg. Chem.*, 2021, **60**, 6911–6921.
- 48 S. De, J. Zhang, R. Luque and N. Yan, *Energy Environ. Sci.*, 2016, **9**, 3314–3347.
- 49 M. H. Tang, C. Hahn, A. J. Klobuchar, J. W. D. Ng, J. Wellendorff, T. Bligaard and T. F. Jaramillo, *Phys. Chem. Chem. Phys.*, 2014, **16**, 19250.
- 50 M. Zhou, C. Li and J. Fang, *Chem. Rev.*, 2021, **121**, 736–795.
- 51 D. Rhuy, Y. Lee, J. Y. Kim, C. Kim, Y. Kwon, D. J. Preston, I. S. Kim, T. W. Odom, K. Kang, D. Lee and W.-K. Lee, *Nano Lett.*, 2022, **22**, 5742–5750.
- 52 D. Strmcnik, P. P. Lopes, B. Genorio and V. R. Stamenkovic, *Nano Energy*, 2016, **29**, 29–36.
- 53 L. Bai, D. A. Harrington and B. E. Conway, *Electrochim. Acta*, 1987, **32**, 1713–1731.
- 54 C. Costentin, S. Drouet, M. Robert and J.-M. Savéant, *J. Am. Chem. Soc.*, 2012, **134**, 11235–11242.
- 55 C. Singh, I. Liberman, R. Shimoni, R. Ifraemov and I. Hod, *J. Phys. Chem. Lett.*, 2019, **10**, 3630–3636.
- 56 A. Kumar, S. Parvin, R. K. Das and S. Bhattacharyya, *Chem.–Asian J.*, 2021, **16**, 3444–3452.
- 57 S. Nitopi, E. Bertheussen, S. B. Scott, X. Liu, A. K. Engstfeld, S. Horch, B. Seger, I. E. L. Stephens, K. Chan, C. Hahn, J. K. Nørskov, T. F. Jaramillo and I. Chorkendorff, *Chem. Rev.*, 2019, **119**, 7610–7672.
- 58 M. Chiesa, E. Giamello and M. Che, *Chem. Rev.*, 2010, **110**, 1320–1347.
- 59 H. Dau, C. Limberg, T. Reier, M. Risch, S. Roggan and P. Strasser, *ChemCatChem*, 2010, **2**, 724–761.
- 60 M. R. Singh, E. L. Clark and A. T. Bell, *Phys. Chem. Chem. Phys.*, 2015, **17**, 18924–18936.
- 61 A. H. Shah, Y. Wang, A. R. Woldu, L. Lin, M. Iqbal, D. Cahen and T. He, *J. Phys. Chem. C*, 2018, **122**, 18528–18536.
- 62 F. Bienen, D. Kopljar, A. Löwe, S. Geiger, N. Wagner, E. Klemm and K. A. Friedrich, *ACS Sustainable Chem. Eng.*, 2020, **8**, 13759–13768.
- 63 T. Murakami, K. Morishita, K. Koike, K. Fujii and S. Wada, *Jpn. J. Appl. Phys.*, 2023, **62**, SK1002.
- 64 B. M. Comer, P. Fuentes, C. O. Dimkpa, Y. H. Liu, C. A. Fernandez, P. Arora, M. Realff, U. Singh, M. C. Hatzell and A. J. Medford, *Joule*, 2019, **3**, 1578–1605.
- 65 Z. Yan, M. Ji, J. Xia and H. Zhu, *Adv. Energy Mater.*, 2020, **10**, 1902020.
- 66 Y. Liu, Y. Su, X. Quan, X. Fan, S. Chen, H. Yu, H. Zhao, Y. Zhang and J. Zhao, *ACS Catal.*, 2018, **8**, 1186–1191.

- 67 F. Hanifpour, C. P. Canales, E. G. Fridriksson, A. Sveinbjörnsson, T. K. Tryggvason, E. Lewin, F. Magnus, Á. S. Ingason, E. Skúlason and H. D. Flosadóttir, *Electrochim. Acta*, 2022, **403**, 139551.
- 68 D. Klotz, *Electrochem. Commun.*, 2019, **98**, 58–62.
- 69 Q. Pang, Y. Zhao, X. Bian, Y. Ju, X. Wang, Y. Wei, B. Liu, F. Du, C. Wang and G. Chen, *J. Mater. Chem. A*, 2017, **5**, 3667–3674.
- 70 M. Weiss, R. Ruess, J. Kasnatscheew, Y. Levartovsky, N. R. Levy, P. Minnmann, L. Stolz, T. Waldmann, M. Wohlfahrt-Mehrens, D. Aurbach, M. Winter, Y. Ein-Eli and J. Janek, *Adv. Energy Mater.*, 2021, **11**, 2101126.
- 71 L. Stolz, M. Gaberšček, M. Winter and J. Kasnatscheew, *Chem. Mater.*, 2022, **34**, 10272–10278.
- 72 B.-A. Mei, J. Lau, T. Lin, S. H. Tolbert, B. S. Dunn and L. Pilon, *J. Phys. Chem. C*, 2018, **122**, 24499–24511.
- 73 S. Nowak and M. Winter, *J. Anal. At. Spectrom.*, 2017, **32**, 1833–1847.
- 74 S. Kobayashi and Y. Uchimoto, *J. Phys. Chem. B*, 2005, **109**, 13322–13326.
- 75 Q.-C. Zhuang, T. Wei, L.-L. Du, Y.-L. Cui, L. Fang and S.-G. Sun, *J. Phys. Chem. C*, 2010, **114**, 8614–8621.
- 76 P. Iurilli, C. Brivio and V. Wood, *J. Power Sources*, 2021, **505**, 229860.
- 77 M. Nakayama, H. Ikuta, Y. Uchimoto and M. Wakihara, *J. Phys. Chem. B*, 2003, **107**, 10603–10607.
- 78 P. G. Bruce and M. Y. Saidi, *J. Electroanal. Chem.*, 1992, **322**, 93–105.
- 79 N. Meddings, M. Heinrich, F. Overney, J.-S. Lee, V. Ruiz, E. Napolitano, S. Seitz, G. Hinds, R. Raccichini, M. Gaberšček and J. Park, *J. Power Sources*, 2020, **480**, 228742.
- 80 N. S. Choi, Z. Chen, S. A. Freunberger, X. Ji, Y. K. Sun, K. Amine, G. Yushin, L. F. Nazar, J. Cho and P. G. Bruce, *Angew. Chem., Int. Ed.*, 2012, **51**, 9994–10024.
- 81 Z. Peng, S. A. Freunberger, L. J. Hardwick, Y. Chen, V. Giordani, F. Bardé, P. Novák, D. Graham, J.-M. Tarascon and P. G. Bruce, *Angew. Chem., Int. Ed.*, 2011, **50**, 6351–6355.
- 82 B. D. McCloskey, A. Speidel, R. Scheffler, D. C. Miller, V. Viswanathan, J. S. Hummelshøj, J. K. Nørskov and A. C. Luntz, *J. Phys. Chem. Lett.*, 2012, **3**, 997–1001.
- 83 M. Haro, N. Vicente and G. Garcia-Belmonte, *Adv. Mater. Interfaces*, 2015, **2**, 1500369.
- 84 M. Haro, T. Song, A. Guerrero, L. Bertoluzzi, J. Bisquert, U. Paik and G. Garcia-Belmonte, *Phys. Chem. Chem. Phys.*, 2014, **16**, 17930.
- 85 R. Majee, Q. A. Islam and S. Bhattacharyya, *ACS Appl. Mater. Interfaces*, 2019, **11**, 35853–35862.
- 86 Y. Guo, P. Yuan, J. Zhang, Y. Hu, I. S. Amiinu, X. Wang, J. Zhou, H. Xia, Z. Song, Q. Xu and S. Mu, *ACS Nano*, 2018, **12**, 1894–1901.
- 87 R. Majee, T. Das, S. Chakraborty and S. Bhattacharyya, *ACS Appl. Mater. Interfaces*, 2020, **12**, 40355–40363.
- 88 B. D. Boruah, A. Mathieson, S. K. Park, X. Zhang, B. Wen, L. Tan, A. Boies and M. De Volder, *Adv. Energy Mater.*, 2021, **11**, 2100115.
- 89 N. F. Yan, G. R. Li and X. P. Gao, *J. Mater. Chem. A*, 2013, **1**, 7012–7015.
- 90 Q. Lv, Z. Zhu, S. Zhao, L. Wang, Q. Zhao, F. Li, L. A. Archer and J. Chen, *J. Am. Chem. Soc.*, 2021, **143**, 1941–1947.
- 91 B. D. Boruah, B. Wen and M. De Volder, *Nano Lett.*, 2021, **21**, 3527–3532.
- 92 B. D. Boruah, B. Wen, S. Nagane, X. Zhang, S. D. Stranks, A. Boies and M. De Volder, *ACS Energy Lett.*, 2020, **5**, 3132–3139.
- 93 Y. Li, Y. Li, A. Pei, K. Yan, Y. Sun, C.-L. Wu, L.-M. Joubert, R. Chin, A. L. Koh, Y. Yu, J. Perrino, B. Butz, S. Chu and Y. Cui, *Science*, 2017, **358**, 506–510.
- 94 C. Deng, H. Wang and S. Wang, *J. Mater. Chem. A*, 2021, **9**, 15734–15743.
- 95 N. Kamboj, B. Debnath, S. Bhardwaj, T. Paul, N. Kumar, S. Ogale, K. Roy and R. S. Dey, *ACS Nano*, 2022, **16**, 15358–15368.
- 96 S. Parvin, D. K. Chaudhary, A. Ghosh and S. Bhattacharyya, *ACS Appl. Mater. Interfaces*, 2019, **11**, 30682–30693.
- 97 B. Debnath, S. Parvin, H. Dixit and S. Bhattacharyya, *ChemSusChem*, 2020, **13**, 3875–3886.
- 98 C. Wang, S. Liu, H. Xu, X. Wang, G. Tian, F. Fan, P. Liu, S. Wang, C. Zeng and C. Shu, *Small*, 2024, 2308995.
- 99 D. Ghosh, D. K. Chaudhary, M. Y. Ali, K. K. Chauhan, S. Prodhan, S. Bhattacharyya, B. Ghosh, P. K. Datta, S. C. Ray and S. Bhattacharyya, *Chem. Sci.*, 2019, **10**, 9530–9541.
- 100 A. Mandal, S. Roy, A. Mondal, S. Gupta, B. Pal and S. Bhattacharyya, *J. Phys. Chem. Lett.*, 2022, **13**, 9103–9113.
- 101 E. von Hauff and D. Klotz, *J. Mater. Chem. C*, 2022, **10**, 742–761.
- 102 Y. Bunga and R. Katakya, *J. Electroanal. Chem.*, 2020, **872**, 114302.
- 103 A. Datta, S. Kapri and S. Bhattacharyya, *Green Chem.*, 2015, **17**, 1572–1580.
- 104 S. P. Chaudhary, S. Bhattacharjee, V. Hazra, S. Shyamal, N. Pradhan and S. Bhattacharyya, *Nanoscale*, 2022, **14**, 4281–4291.
- 105 S. Zhu, X. Sun, Y. Wang, N. Zhao and J. Sha, *J. Electroanal. Chem.*, 2019, **855**, 113627.
- 106 P. Vadhma, J. Hu, M. J. Johnson, R. Stocker, M. Braglia, D. J. L. Brett and A. J. E. Rettie, *ChemElectroChem*, 2021, **8**, 1930–1947.
- 107 S. Buteau and J. R. Dahn, *J. Electrochem. Soc.*, 2019, **166**, A1611–A1622.
- 108 A. Sahasrabudhe and S. Bhattacharyya, *Chem. Mater.*, 2015, **27**, 4848–4859.
- 109 B. Bera, A. Chakraborty, T. Kar, P. Leuaa and M. Neergat, *J. Phys. Chem. C*, 2017, **121**, 20850–20856.
- 110 D. Ghosh, S. Kapri and S. Bhattacharyya, *ACS Appl. Mater. Interfaces*, 2016, **8**, 35496–35504.
- 111 A. Datta, S. Kapri and S. Bhattacharyya, *J. Mater. Chem. A*, 2016, **4**, 14614–14624.
- 112 R. Singhal, Z. Orynbayeva, R. V. K. Sundaram, J. J. Niu, S. Bhattacharyya, E. A. Vitol, M. G. Schrlau, E. S. Papazoglou, G. Friedman and Y. Gogotsi, *Nat. Nanotechnol.*, 2011, **6**, 57–64.

Perspective

- 113 A. Datta, A. Sadhu, S. Santra, S. M. Shivaprasad, S. K. Mandal and S. Bhattacharyya, *Chem. Commun.*, 2014, **50**, 10510–10512.
- 114 N. Leibowitz, J. Schiffbauer, S. Park and G. Yossifon, *Phys. Rev. E*, 2018, **97**, 043104.
- 115 J. Schiffbauer, U. Liel and G. Yossifon, *Phys. Rev. E: Stat., Nonlinear, Soft Matter Phys.*, 2014, **89**, 033017.
- 116 R. Singhal, S. Bhattacharyya, Z. Orynbayeva, E. Vitol, G. Friedman and Y. Gogotsi, *Nanotechnology*, 2010, **21**, 015304.
- 117 J. P. Neto, P. Baião, G. Lopes, J. Frazão, J. Nogueira, E. Fortunato, P. Barquinha and A. R. Kampff, *Front. Neurosci.*, 2018, **12**, 715.